The Journal of the Astronautical Sciences (2026) 73:47
https://doi.org/10.1007/s40295-026-00599-7

RESEARCH

Momentum Management of a Spacecraft Equipped with a Dual-Gimbaled Electric Thruster and Rotating Solar Arrays

Riccardo Calaon[1] · Cody Allard[2] · Hanspeter Schaub[1]

Received: 22 September 2025 / Accepted: 13 May 2026

Abstract

Unmodeled forces and torques can cause significant variations in the desired position and attitude of a spacecraft in orbit. For the attitude part, disturbances are typically absorbed by reaction wheels, which have the ability to store external torques in the form of angular momentum. This paper investigates the use of a gimbaled solar electric propulsion thruster to manage reaction wheel momentum, in addition to its primary scope of providing low thrust to follow a heliocentric trajectory, with the aim to prevent the wheel momentum from growing excessively. The thruster is mounted on a dual-gimbaled platform attached to the spacecraft hub. The two degrees of freedom associated with the direction of the thruster are exploited to counteract the momentum buildup on the wheels and reduce the necessity of performing impulsive momentum management. The novelty of this work is the complete kinematic analysis of this system for general spacecraft configurations with such a gimbaled thruster. Large rotating solar arrays provide the required power for the electric thruster and are also used to leverage the solar radiation pressure torque to offload momentum. Emphasis is placed on the problem of determining how to align the thruster in the presence of uncertainties in the center of mass location. The steady-state integral feedback term of the attitude control law is used to inform a sequential least-squares estimator about the location of the center of mass, which is iteratively estimated. The results illustrate that even with small degree-level thruster platform orientation changes, the three-dimensional center-of-mass location can be estimated.

✉ Riccardo Calaon
riccardo.calaon@colorado.edu

Cody Allard
cody.allard@lasp.colorado.edu

Hanspeter Schaub
hanspeter.schaub@colorado.edu

[1] Ann and H. J. Smead Department of Aerospace Engineering Sciences, Colorado Center for Astrodynamics Research, 3775 Discovery Drive, Boulder 80303, CO, United States

[2] Laboratory for Atmospheric and Space Physics, 1234 Innovation Drive, Boulder 80303, CO, United States

Published online: 01 June 2026

Keywords Momentum management · Gimbaled thruster · Rotating solar arrays · Basilisk · Spacecraft · Lyapunov control

1 Introduction

Modern spacecraft designs often involve the presence of electric thrusters given their high specific impulse and, consequently, lower propellant mass requirement [1]. On the downside, the spacecraft needs to produce enough electrical power to sustain such electric thrusters. For spacecraft orbiting Earth or orbiting the Sun within the inner part of the Solar System, this requirement often translates into the necessity of equipping the spacecraft with very large solar arrays to meet the power demand. This, on the other hand, makes the effects of the solar radiation pressure (SRP) acting on the spacecraft system significantly stronger, as large solar arrays can act like solar sails that can cause the spacecraft to drift away from the nominal attitude [2]. The attitude of the spacecraft is often designed to meet a series of pointing requirements and therefore must be maintained within a certain accuracy. For this reason, the torque resulting from SRP, as well as other unmodeled external torques, is typically absorbed by momentum exchange devices such as reaction wheels (RWs) or control moment gyros (CMGs). These actuators are spun up and down to exchange momentum with the spacecraft and perform attitude maneuvers, or, conversely, they can hold the spacecraft attitude in place while absorbing external torques [3]. In the second case, because external torques act on the system, the angular momentum is accumulated on the actuators, rather than on the spacecraft hub. This can be done up to a certain point, because significant problems arise when RWs or CMGs are spun at very high angular rates. First, this causes mechanical stress on the bearings and significant power consumption. Second, a high accumulated momentum makes it increasingly harder to control the spacecraft, requiring a larger torque from the actuators, which might in return not be able to deliver it.

For the aforementioned reasons, momentum management is a necessary part of mission design. Here, external torques are delivered to the system so that the resulting variation in net momentum reduces the angular velocities of the wheels. In the most general case, this is done through a set of thrusters located on the main hub, typically in pairs, to avoid producing net forces on the system that could cause trajectory deviations. This choice is associated with an additional use of propellant mass and also with the problem of high-frequency oscillation caused by the thruster firing. The firing of on-off thrusters can excite the vibrational modes of long appendages, such as the solar arrays [4] or require accurate positioning of the payload [5]. Another problem related to performing momentum dumping using thrusters is the fact that one or more of them might fail. For this reason, there exists work in the literature that addresses how to dump momentum using alternative underactuated control torques [6]. In this case, however, momentum dumping occurs over multiple phases that require attitude reorientation, and therefore, the temporary loss of the reference attitude. Other existing work investigates how to continuously manage momentum build-up exploiting environment features, such as the gravity gradient torque [7], or Earth's magnetic field,

by means of onboard magnetorquers [8]. However, both these approaches are only applicable for Earth-orbiting satellites and not for deep-space missions.

Some of the more recent mission designs have explored the idea of mounting the electric thruster on a dual-gimbal mechanism that allows to control the direction of the thrust vector with respect to the spacecraft hub. In principle, this is motivated by the need to adjust the thrust direction based on the system center of mass as it changes over time [9, 10] and avoid additional momentum accumulation due to a thruster misalignment. However, this design can be leveraged to take an additional step forward, by intentionally offsetting the thruster with respect to the center of mass in order to produce a counterbalancing torque on the system that can offload the momentum accumulated due to external perturbations. A similar concept has been implemented for the recent Psyche mission, involving two such thrusters, each mounted on a dual gimbal [11], and similarly it is the driving design for the Emirates Mission to the Asteroid Belt [12, 13]. The use of gimbaled electric thrusters to perform momentum management, sometimes in combination with exploitation of external perturbations such as SRP, have been discussed before [14, 15] and implemented in missions like Hayabusa 1 and 2 and BepiColombo. The Hayabusa spacecraft, however, featured hard-mounted solar arrays: SRP was leveraged passively, as a stabilizing torque that allowed to maintain Sun pointing configuration while cancelling other perturbations [16]. The BepiColombo spacecraft, on the other hand, made a more deliberate use of the torque available through SRP exploitation using articulated solar arrays. In the BepiColombo mission, arrays were actuated in order to produce control torques that offloaded the reaction wheels, in a similar fashion to what is proposed in this work [17]. The main difference between the approach presented in this paper and the BepiColombo mission consists of the concurrent use of the gimbaled SEP thruster and rotating solar arrays for momentum management, which in the architecture presented here constitute a full, three-axial control strategy. The BepiColombo spacecraft, in contrast, leveraged the SRP on the rotating arrays in combination with chemical propulsion for momentum management, without fully exploiting the SEP thruster's torquing capability. Even for approaches that apply very similar ideas and designs to those presenting in this paper, the existing literature could benefit from an expansion on detailed analytical derivations of the guidance and control laws required for such applications and their stability, as well as simulation results considering fully-coupled system dynamics.

Whether the goal is to perform continuous momentum management, or to produce zero net torque on the system, accurate knowledge of the location of the center of mass of the spacecraft system is needed to fire the thruster along the right direction. Mass properties are often estimated by performing calibration maneuvers, during which the large angular rates and accelerations of the slewing spacecraft are measured and constitute the observations for several Kalman filters that provide updated estimates of the inertia tensor, the location of the center of mass, and the total system mass [18, 19]. These filters combine measurements from onboard instruments with first principles, such as conservation of angular momentum [20]. However, such maneuvers require specific calibration procedures that involve large slews that can interrupt the spacecraft's nominal operations [21] and once again excite the vibrational modes of flexible components. Finally, rotating calibration maneuvers can agitate the fuel inside the tanks, which would otherwise tend to accumulate along the thrust direction as a

result of the propulsive thrust. Other methods for estimating inertia properties involve articulation of moving appendages: accurate knowledge of the mass and position of the appendage with respect to the body, combined with velocity measurements, allows to estimate the inertia properties for the whole system [22]. This work aims to propose a CM estimation algorithm that works concurrently with the momentum management techniques proposed in this article, in order to quickly converge on a CM estimate without performing ad-hoc calibration maneuvers that would otherwise interrupt the flow of spacecraft operations.

This work considers a spacecraft on a heliocentric orbit, propelled by a solar electric propulsion (SEP) thruster. The thruster is mounted on a platform that is connected to the spacecraft hub via a two-axis gimbal that enables tip-and-tilt type of rotations. Additionally, the spacecraft features two solar arrays attached to the hub via one-degree-of-freedom hinges, which allow the arrays to rotate about the hinge axis to maximize illumination. The first goal of this paper is to articulate the platform to align the thrust direction with the center of mass (CM), when the desire is to not produce a net torque on the system. Secondly, this paper looks into designing a control algorithm that aligns the thruster at an offset with respect to the system CM, to have the resulting torque counteract the momentum building up on the wheels due to SRP. In a similar fashion, this paper proposes a control law to differentially articulate symmetric solar arrays to exploit the resulting SRP torque to further offload the system momentum. The stability of the momentum management control laws is proved via nonlinear Lyapunov control theory. Lastly, this paper proposes a technique to continuously estimate the CM location of the system while the thrust is continuously applied. The motion platform supporting the thruster is periodically gimbaled to align the thrust vector based on the current CM estimate. Of interest is how these small platform orientation changes can be used to make the three-dimensional CM location observable. In this work, the steady-state response of the attitude control system with integral feedback constitutes the measurement model to inform the estimator on the torque produced by the offset between CM and thrust vector. The steady-state integral feedback term accounts for the net external torque acting on the spacecraft system. The CM location is updated assuming that this term is dominated by the thruster torque caused by CM uncertainty, but it also considers the torques due to other external influences, like SRP itself. The analysis explores the effectiveness of this approach in an integrated mission scenario that enforces the inertial thruster pointing constraint and corrects the body and platform orientations to seek long-term thrusting without reaction wheel momentum build-up.

This paper is structured as follows: first, the system dynamics are described in Section 2, with an emphasis on the control laws used to actuate the different components. Section 3 describes an analytical closed-form solution to drive the thruster-platform assembly through the desired point within the spacecraft. Section 4 and 5 then expand on this solution to deliver control laws that can feed back on net RW momentum to perform continuous, 3-axis momentum management. Section 6 outlines a least-squares algorithm that allows continuous CM estimation based on integral feedback torque. Section 7 describes the details of the simulated spacecraft, such as mass properties and initial conditions. The simulation results are presented in Section 8, and conclusions are drawn in Section 9.

2 System Dynamics

The spacecraft analyzed in this paper features several components. The main component is the rigid spacecraft hub, whose motion affects the dynamics of all connected components. The rotational motion of the hub is controlled by means of four reaction wheels in a pyramidal configuration. The solar arrays and the gimbaled platform, on which the electric thruster is mounted, are modeled as rigid bodies connected to the hub by means of hinges that can exchange forces and torques with the hub. Simulating a spacecraft featuring moving components is a nontrivial challenge because of the coupled nature of the equations of motion that govern the dynamics of each individual component. This work is based on the modular software architecture presented by Allard et al. [23], which retains the fully coupled nature of the equations of motion while solving the rotational and translational dynamics of the hub first and for the relative dynamics of the moving components second.

The purpose of this section is to outline the equations of motion and control laws that govern the dynamics of each individual component, and ultimately, to detail how the interactions between these dynamic components impact the motion of the spacecraft as a whole. The vector notation used throughout this paper is the following: (i) left superscripts refer to the frame a certain vector is expressed in; in the absence of a left superscript, the equation is valid irrespectively of the frame; (ii) right subscripts describe the property of a frame with respect to another frame (es: $\boldsymbol{\omega}_{\mathcal{B}/\mathcal{N}}$ is the angular velocity of frame $\mathcal{B}$ with respect to frame $\mathcal{N}$); (iii) the hat operator $\hat{}$ denotes a unit vector; and (iv) the tilde operator $\tilde{}$ denotes the skew-symmetric cross product matrix. Terms between square brackets are matrices.

2.1 Spacecraft Hub

With respect to Figure 1, the frame $\mathcal{N} = \{\hat{\boldsymbol{n}}_1, \hat{\boldsymbol{n}}_2, \hat{\boldsymbol{n}}_3\}$ is the inertial frame. The body frame $\mathcal{B} = \{\hat{\boldsymbol{b}}_1, \hat{\boldsymbol{b}}_2, \hat{\boldsymbol{b}}_3\}$ with origin in point B is fixed with respect to the hub, and it is the frame in which the spacecraft attitude $\boldsymbol{\sigma}_{\mathcal{B}/\mathcal{N}}$, angular rates $\boldsymbol{\omega}_{\mathcal{B}/\mathcal{N}}$, and angular accelerations $\dot{\boldsymbol{\omega}}_{\mathcal{B}/\mathcal{N}}$ are defined with respect to the inertial frame. The attitude representation adopted in this work and denoted with the letter $\boldsymbol{\sigma}$ is Modified Rodrigues Parameters (MRPs) [24]. The feedback control law implemented to control the attitude of the hub is a nonlinear, second-order PID-like controller based on the MRP attitude formulation [3]:

$$\begin{aligned}\boldsymbol{u} &= -K\boldsymbol{\sigma}_{\mathcal{B}/\mathcal{R}} - P\boldsymbol{\omega}_{\mathcal{B}/\mathcal{R}} - PK_I\boldsymbol{z} + \\ &+\boldsymbol{\omega}_{\mathcal{B}/\mathcal{N}} \times \left([\boldsymbol{J}_{\text{tot},C}]\boldsymbol{\omega}_{\mathcal{B}/\mathcal{N}} + [\boldsymbol{G}_s]\boldsymbol{h}_s\right) + [\boldsymbol{J}_{\text{tot},C}]\left(\dot{\boldsymbol{\omega}}_{\mathcal{R}/\mathcal{N}} - \boldsymbol{\omega}_{\mathcal{B}/\mathcal{N}} \times \boldsymbol{\omega}_{\mathcal{R}/\mathcal{N}}\right)\end{aligned} \tag{1}$$

where the first three terms constitute, respectively, the proportional, derivative, and integral terms, K, P, and K_I are scalar control gains, and vector $\boldsymbol{z}$ is defined as [25]:

$$\boldsymbol{z} = K\int_{t_0}^{t} \boldsymbol{\sigma}_{\mathcal{B}/\mathcal{R}}\mathrm{d}t + [\boldsymbol{J}_{\text{tot},C}]\boldsymbol{\omega}_{\mathcal{B}/\mathcal{R}}. \tag{2}$$

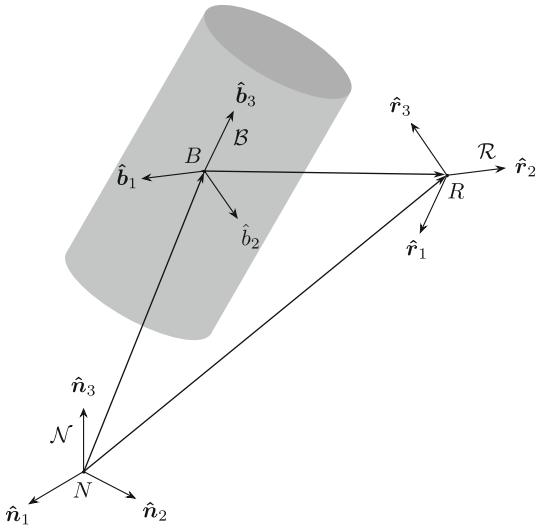

Fig. 1 Body, Reference, and Inertial frames

The other terms arise due to the gyroscopic couplings in Euler's equation of motion and are needed in the nonlinear control law to ensure asymptotic stability. The tensor $[\boldsymbol{J}_{\text{tot},C}]$ represents the inertia of the entire system, minus the inertias of the reaction wheels about their respective spin axes. See Schaub and Junkins [3] for a detailed derivation of this control law. The term $[\boldsymbol{G}_s]\boldsymbol{h}_s$ describes the angular momentum contribution of the reaction wheels, and it is described in the next subsection. The frame $\mathcal{R} = \{\hat{\boldsymbol{r}}_1, \hat{\boldsymbol{r}}_2, \hat{\boldsymbol{r}}_3\}$ is the reference frame for the hub, that is, a frame that the body frame must be driven to, in order to comply with mission pointing requirements. The problem of defining the optimal reference frame for a spacecraft with multiple pointing requirements is discussed in Calaon et al. [26]. It is important to note that the tensor $[\boldsymbol{J}_{\text{tot},C}]$ is, in general, not constant, because it factors in the inertias of moving components such as the arrays and the thruster platform. Uncertainties on the inertias of the individual components, combined with uncertainties on the relative position between them, can make this tensor difficult to estimate. The control law in Equation Equation (1) is designed to zero the relative attitude $\boldsymbol{\sigma}_{\mathcal{B}/\mathcal{R}}$ and angular velocity $\boldsymbol{\omega}_{\mathcal{B}/\mathcal{R}}$ between the body frame $\mathcal{B}$ and a reference frame $\mathcal{R}$. The integral term $PK_I\boldsymbol{z}$ has the ability to zero the bias in the steady-state response due to a constant unmodeled torque acting on the system. As will be further discussed later in the paper, the integral feedback term fits well within the purpose of this work, where the assumption is that the unmodeled torques acting on the system are dominated by the torque produced by the thruster offset with respect to the system's CM. When the thruster force and its application point, in first approximation, do not vary in time, the assumption of a constant unmodeled torque is consistent.

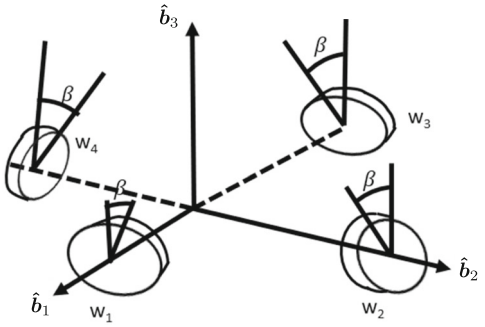

Fig. 2 Four reaction wheels in pyramid configuration [27]

2.2 Reaction Wheels

Figure 2 shows the reaction wheel setup for the spacecraft hub. The RWs are installed so that two reaction wheels can provide torque about the first principal body axis ${}^{\mathcal{B}}\hat{\boldsymbol{b}}_1 = \{1, 0, 0\}^T$, two about the second principal body axis ${}^{\mathcal{B}}\hat{\boldsymbol{b}}_2 = \{0, 1, 0\}^T$, and all four contribute to the torque about the third principal body axis ${}^{\mathcal{B}}\hat{\boldsymbol{b}}_3 = \{0, 0, 1\}^T$. This is achieved by a 40 degree upward tilt angle in the direction of the wheels' spin axes $\hat{\boldsymbol{u}}_j$, and it is done to ensure that control about each axis is achievable even in the case of a single wheel failure.

Given the following matrix $[\boldsymbol{G}_s] = \{{}^{\mathcal{B}}\hat{\boldsymbol{u}}_1, {}^{\mathcal{B}}\hat{\boldsymbol{u}}_2, {}^{\mathcal{B}}\hat{\boldsymbol{u}}_3, {}^{\mathcal{B}}\hat{\boldsymbol{u}}_4\}$ and under the assumption that the center of mass of each wheel is aligned with the respective spin axis, the rotational equations of motion of the wheels are given by:

$$\boldsymbol{u}_{\mathrm{RW}} = \dot{\boldsymbol{h}}_s = J_{\mathrm{W}}(\dot{\boldsymbol{\Omega}} + [\boldsymbol{G}_s]^T \dot{\boldsymbol{\omega}}_{\mathcal{B}/\mathcal{N}}) \tag{3}$$

where $\boldsymbol{\Omega}$ is the array of wheel speeds and J_{W} is the inertia of the wheels about their respective spin axes. The torques to the individual reaction wheels are computed by means of the minimum-norm solution, based on the requested torque in Equation (1):

$$\boldsymbol{u}_{\mathrm{RW}} = -[\boldsymbol{G}_s]^T \left([\boldsymbol{G}_s][\boldsymbol{G}_s]^T\right)^{-1} \boldsymbol{u} \tag{4}$$

where $\boldsymbol{u}$ is the torque being exchanged between the RWs and the hub. Because the wheels are balanced and their respective axes do not change with respect to the hub, the wheels' dynamics do not affect the location of the CM of the system over time. In a more refined scenario, it is possible to simulate the static and dynamic imbalance of the wheels while solving for the fully coupled dynamics of the system [28].

2.3 Rotating Solar Arrays

Each solar array is modeled as a rigid body attached to the hub by means of a single degree-of-freedom hinge. Rotations about the hinge are aimed to track the direction of incoming sunlight. With respect to Figure 3, frame $\mathcal{A} = \{\hat{\boldsymbol{a}}_1, \hat{\boldsymbol{a}}_2, \hat{\boldsymbol{a}}_3\}$ is fixed within

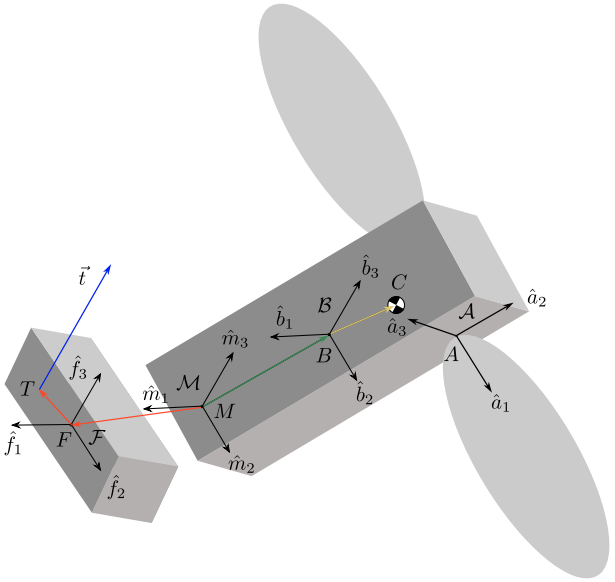

Fig. 3 Spacecraft and gimbaled thruster sketch

each solar array; however, the spin axis $\hat{\boldsymbol{a}}_1$ is also fixed with respect to the body frame $\mathcal{B}$, while $\hat{\boldsymbol{a}}_2$ is orthogonal to the power-generating surface of the array, and is ideally pointed in the direction of the Sun. Solar array flexing is not modeled in this work: for details on how to model first-order flexing in a modular way, the reader is referred to Allard et al. [29].

The motion of the system consisting of the hub and solar arrays is described by a system of three equations that relate to the translational motion of the CM of the system, three equations that relate to the rotation of the system, plus one equation for each solar array that describes the additional degree of freedom that enables the arrays to rotate about their hinge axis. The analytical derivation of the equations of motion is lengthy and out of the scope of this paper. For details, the reader is referred to Carneiro et al. [30], which describes how to implement the backsubstitution method to solve for the equations of motion of a coupled system in a very compact way. For the purpose of this analysis, the focus is on the fact that the relative rotation between the hub and the arrays is controlled via a torque input. This is the torque exchanged between the hub and each array, and it has the form of a PD control law:

$$\boldsymbol{u}_{\mathrm{SA}} = -\left[K_{\mathrm{SA}}(\alpha - \alpha_R) + P_{\mathrm{SA}}(\dot{\alpha} - \dot{\alpha}_R)\right]\hat{\boldsymbol{a}}_1 \tag{5}$$

where α is the relative angle between hub and array(s) at nominal pose, and α_R is the reference angle that ensures maximum sunlight incidence on the array surface. The derivation of α_R is also found in Calaon et al. [26]. In this work, the center of mass of the arrays is aligned with the spin axis, therefore the motion of the arrays does not affect the location of the CM of the system.

2.4 Gimbaled Thruster Platform

The thruster-platform assembly is modeled as a rigid body attached to the bottom surface of the spacecraft. A two-axis gimbal connects the platform to the main hub, allowing it to perform tip and tilt rotations with respect to the hub. In this case, two differential equations are required to describe the dynamics of the gimbal with respect to the hub, on top of the six equations that describe the translational motion of the CM and the rotation of the system. The thruster-platform assembly is modeled analogously to the solar arrays, with the exception that there are, in this case, two degrees of freedom between the hub and the platform. The equations of motion are once again solved using the back-substitution method [30]. The two gimbal angles ν_1 and ν_2 are also controlled via torque inputs about the gimbal axes, once again according to PD control laws:

$$\boldsymbol{u}_{\mathrm{PL}} = -\left[K_{\mathrm{PL}}(\nu_1 - \nu_{R1}) + P_{\mathrm{PL}}(\dot{\nu}_1 - \dot{\nu}_{R1})\right]\hat{\boldsymbol{m}}_1 - \left[K_{\mathrm{PL}}(\nu_2 - \nu_{R2}) + P_{\mathrm{PL}}(\dot{\nu}_2 - \dot{\nu}_{R2})\right]\hat{\boldsymbol{f}}_2. \tag{6}$$

More details on the mount frame $\mathcal{M} = \{\hat{\boldsymbol{m}}_1, \hat{\boldsymbol{m}}_2, \hat{\boldsymbol{m}}_3\}$ and the platform frame $\mathcal{F} = \{\hat{\boldsymbol{f}}_1, \hat{\boldsymbol{f}}_2, \hat{\boldsymbol{f}}_3\}$, as well as how to compute the reference angles, are provided in Section 3. It is important to note that the thrust vector $\boldsymbol{t}$ is defined in platform frame coordinates, as the thrust force is applied to the platform. However, applying the backsubstitution method, the force and torque resulting from the thruster's action are mapped into resulting force and torque on the system as a whole.

2.5 Combined Equations of Motion

All of the components described above interact with each other through the exchange of forces and torques. To correctly describe the dynamics of the system in all its parts, 14 equations of motion are required. The equations of motion for the translation of the system are not relevant in this work. The rotational equations can be simplified considering the steady-state response of the solar arrays and thruster platform. In the absence of parasitic torques acting about the hinges and gimbals that connect these components to the hub, both Equation (5) and (6) are proven to drop to zero once the desired reference angles are tracked, therefore they do not contribute to the steady-state equations of motion. PD controls are chosen for the arrays and the thruster platform for implementation simplicity, and the control gains are tuned in order to ensure a faster convergence time than the hub attitude. This, however, is not a requirement, and a different type of control can be modeled without affecting the validity of the results of this paper. An example of how to implement prescribed motion actuators dynamics using, for example, stepper motors, can be found in Kiner et al. [31].

The resulting steady-state rotational equations of motion for the combined system are:

$$[\boldsymbol{J}_{\mathrm{tot},C}]\dot{\boldsymbol{\omega}}_{\mathcal{B}/\mathcal{N}} = -\boldsymbol{\omega}_{\mathcal{B}/\mathcal{N}} \times ([\boldsymbol{J}_{\mathrm{tot},C}]\boldsymbol{\omega}_{\mathcal{B}/\mathcal{N}} + [\boldsymbol{G}_s]\boldsymbol{h}_s) + \boldsymbol{L}_{\mathrm{thr}} + \boldsymbol{L}_{\mathrm{ext}} + \boldsymbol{u} \tag{7}$$

where $\boldsymbol{u}$ is the control torque applied to the hub, as per Equation (1) and $[\boldsymbol{J}_{\mathrm{tot},C}]$ is, again, the inertia of the entire system at steady state, minus the inertias of the RWs

about their respective spin axes. Under the assumption that the solar arrays and the platform have reached their steady-state position, it is valid to assume that $[\boldsymbol{J}_{\text{tot},C}]$ is constant in Equation (7), and that the system as a whole can be effectively treated as a rigid body. Equation (3) provides the dynamics of the four reaction wheels. The term $\boldsymbol{L}_{\text{ext}}$ consists of any unmodeled external torque acting on the system. In this work, it corresponds to the SRP toque on the spacecraft. Lastly, $\boldsymbol{L}_{\text{thr}}$ is the torque that the thruster produces on the system, and it is further discussed in Section 6.

3 Gimbaled Platform Guidance

The platform supporting the electric thruster is modeled as a rigid body attached to the main spacecraft hub, as shown in Figure 3. To describe the relative motion between the two, two frames are defined: frame $\mathcal{M} = \{\hat{\boldsymbol{m}}_1, \hat{\boldsymbol{m}}_2, \hat{\boldsymbol{m}}_3\}$ is a hub-fixed frame, whose origin M coincides with the joint through which the platform and hub are connected and exchange forces. The frame $\mathcal{F} = \{\hat{\boldsymbol{f}}_1, \hat{\boldsymbol{f}}_2, \hat{\boldsymbol{f}}_3\}$, with origin F, is a platform-fixed frame. The complexity of the problem involving the articulation of the platform lies in the fact that the thrust vector is expressed in $\mathcal{F}$-frame coordinates and applied through point T, which may not coincide with the origin F of the frame. Furthermore, the origins of the two frames M and F, in general, do not coincide either. This section describes how to compute the reference gimbal angles ν_{R1} and ν_{R2} that align the thrust direction unit vector $\hat{\boldsymbol{t}}$, expressed in $\mathcal{F}$-frame coordinates, through a specific point C in the hub. This point C can coincide with the system's CM, if the desire is to have the thrust not produce a torque on the system. Conversely, it is possible to intentionally thrust at an offset distance from the center of mass to exploit such a torque to perform momentum management. This section does not consider the uncertainty on the location of point C as, for this analysis, the assumption is that the coordinates of point C are known. The final direction cosine matrix that aligns the thrust with the desired point C is obtained through a series of three consecutive rigid body rotations that take advantage of intermediate frames.

3.1 Gimbaled platform and thruster modeling

The relative motion between the platform and the hub consists of 2 degrees of freedom tip-and-tilt rotations. Such rotation angles ν_1 and ν_2 are defined about the $\hat{\boldsymbol{m}}_1$ axis and the intermediate $\hat{\boldsymbol{f}}_2$ axis, respectively, via two consecutive rotations. The direction cosine matrix that defines the mapping from $\mathcal{M}$ to $\mathcal{F}$ is therefore:

$$[\mathcal{F}\mathcal{M}] = \begin{bmatrix} \cos\nu_2 & \sin\nu_1 \sin\nu_2 & -\cos\nu_1 \sin\nu_2 \\ 0 & \cos\nu_1 & \sin\nu_1 \\ \sin\nu_2 & -\sin\nu_1 \cos\nu_2 & \cos\nu_1 \cos\nu_2 \end{bmatrix} \tag{8}$$

where emphasis is put on the fact that the element (2, 1) of the $[\mathcal{F}\mathcal{M}]$ direction cosine matrix must be zero. This ensures that the rotation is, in fact, a tip-and-tilt type of rotation that is compliant with the constrained motion of the platform. Moreover, it

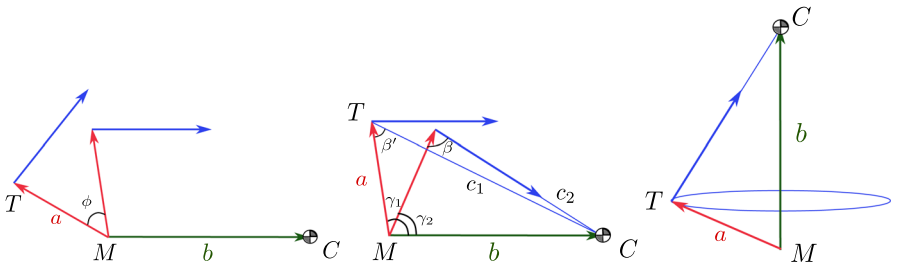

(a) First rotation (b) Second rotation (c) Third rotation

Fig. 4 Three consecutive rotations

can be observed that when $\nu_1 = \nu_2 = 0$ the two frames align and the mapping becomes an identity.

To solve the problem in its most general form, the following offset vectors are defined:

- ${}^{\mathcal{M}}\boldsymbol{r}_{C/M}$: position of C with respect to M, expressed in $\mathcal{M}$-frame coordinates;
- ${}^{\mathcal{F}}\boldsymbol{r}_{F/M}$: position of F with respect to M, expressed in $\mathcal{F}$-frame coordinates;
- ${}^{\mathcal{F}}\boldsymbol{r}_{T/F}$: position of T with respect to F, expressed in $\mathcal{F}$-frame coordinates.

For ease of notation, the following vector are defined and used in the following subsections:

$$\boldsymbol{a} = \boldsymbol{r}_{F/M} + \boldsymbol{r}_{T/F} \qquad \boldsymbol{b} = \boldsymbol{r}_{C/M}. \tag{9}$$

3.2 First rotation

The first rotation is defined starting from the hub-fixed frame $\mathcal{M}$, and it maps to an intermediate frame $\mathcal{D}_1$ such that, when $\mathcal{F} \equiv \mathcal{D}_1$, the thrust vector $\boldsymbol{t}$ is parallel to $\boldsymbol{b}$. The DCM $[\mathcal{D}_1\mathcal{M}]$ is defined by means of the principal rotation angle and the principal rotation vector $(\phi, \hat{\boldsymbol{e}}_\phi)$. These quantities are computed as follows:

$$\phi = \arccos\left(\frac{{}^{\mathcal{F}}\boldsymbol{t} \cdot {}^{\mathcal{M}}\boldsymbol{b}}{\|\boldsymbol{t}\| \cdot \|\boldsymbol{b}\|}\right) \qquad \hat{\boldsymbol{e}}_\phi = \frac{{}^{\mathcal{F}}\boldsymbol{t} \times {}^{\mathcal{M}}\boldsymbol{b}}{\|{}^{\mathcal{F}}\boldsymbol{t} \times {}^{\mathcal{M}}\boldsymbol{b}\|}. \tag{10}$$

The mapping $[\mathcal{D}_1\mathcal{M}] = f(\phi, \hat{\boldsymbol{e}}_\phi)$ from principal rotation sets to DCM is a classc result of rigid body dynamics, and its formulation can be traced back to the work by Rodrigues [32]. Figure 4(a) visually shows the rotation of vectors performed by the first DCM. It should be noted that the matrix $[\mathcal{D}_1\mathcal{M}]$ is, in general, not constraint compliant, i.e., it does not describe a tip-and-tilt rotation like the DCM outlined in Equation (8).

3.3 Second rotation

The second rotation places the thrust direction vector through point C. The principal rotation vector in this case is again $\hat{\boldsymbol{e}}_\psi = \hat{\boldsymbol{e}}_\phi$, so the rotation is a direct continuation of the previous one. However, the derivation of the second principal rotation angle ψ is significantly less intuitive. When the thrust application point T coincides with the origin of the hub-fixed frame M, therefore $\|\boldsymbol{a}\| = 0$, it is also $\psi = 0$, and the first rotation alone is sufficient to place the thrust through point C. When this is not the case, the non-zero value of ψ must be computed. Figure 4(b) shows the second rotation that aligns the thrust vector, in blue and initially parallel to $\boldsymbol{b}$, to point C. The principal rotation angle ψ is obtained as $\psi = \gamma_1 - \gamma_2$. The angles β, β' and γ_1 are known from the geometry and the relative position of the vectors at the beginning of the second rotation. The segments c_1 and c_2, respectively the distance between the thrust application point T and point C before and after the rotation, are computed as follows:

$$c_1 = \sqrt{a^2 + b^2 - 2ab\cos\gamma_1} \qquad c_2 = a\cos\beta \pm \sqrt{b^2 - a^2\sin^2\beta}. \tag{11}$$

It can be observed that c_2 only exists when the relation $b \geq a|\sin\beta|$ is satisfied. This means that it might not always be possible to align the thrust vector with point C for any choice of vectors $\boldsymbol{a}$ and $\boldsymbol{b}$. Taking the product of the two solutions for c_2 given in Equation (11) gives:

$$c_{2,1} \cdot c_{2,2} = a^2\cos^2\beta - b^2 + a^2\sin^2\beta = a^2 - b^2 \tag{12}$$

which is negative when $a < b$. This is considered a valid assumption for the following reasons: vector $\boldsymbol{b}$ indicates the position of point C, which in general coincides with the CM of the system, with respect to point M. For a massive spacecraft, the system CM is located close to the geometric center of the system, thus away from point M, which is at the lower end of the hub where the platform is attached. Vector $\boldsymbol{a}$, on the contrary, is the offset between the thrust application point T and point M. Considering the thruster-platform assembly relatively small compared to the spacecraft hub makes $a < b$ a reasonable assumption. With these considerations, the choice for c_2 is:

$$c_2 = a\cos\beta + \sqrt{b^2 - a^2\sin^2\beta}. \tag{13}$$

The principal rotation angle γ is derived from trigonometric relations:

$$\begin{aligned}\sin\psi &= \sin(\gamma_1 - \gamma_2) = \cos\gamma_2\sin\gamma_1 - \cos\gamma_1\sin\gamma_2 \\ &= \frac{1}{b}(c_1\cos\gamma_2\sin\beta' - c_2\cos\gamma_1\sin\beta)\end{aligned} \tag{14}$$

with:

$$\cos\gamma_i = \frac{a^2 + b^2 - c_i^2}{2ab} \qquad \text{for} \qquad i = 1, 2. \tag{15}$$

Ultimately, the second DCM is derived as $[\mathcal{D}_2\mathcal{D}_1] = f(\psi, \hat{\boldsymbol{e}}_\psi)$. Multiplying the first and second rotation matrices gives the DCM:

$$[\mathcal{D}_2\mathcal{M}] = [\mathcal{D}_2\mathcal{D}_1][\mathcal{D}_1\mathcal{M}] \tag{16}$$

where again, in general, $[\mathcal{D}_2\mathcal{M}]$ does not describe a rotation that is compliant with the constraints expressed by Equation (8).

3.4 Third Rotation

The first two rotations show that it is possible, under reasonable assumptions, to rotate the thrust vector in order to align it with point C in the hub. However, it is not yet possible to do so through a rotation that is also compliant with the platform's constraints, which only allow tip-and-tilt kind of rotations. This subsection computes a third rotation DCM that maintains the alignment condition achieved by the first two rotations, and simultaneously enforces the constraint compliance on the final solution. Equation (16) provides a rotation matrix that puts the thrust vector through point C, but this solution is not unique. In fact, there exists a family of infinite DCMs that accomplish the same result. Of all such DCMs, the purpose of this subsection is to find the one that is also constraint-compliant. Let us define such a DCM as $[\mathcal{D}_3\mathcal{M}]$. Figure 4(c) shows that rotations about the $\boldsymbol{b}$ vector do not break the desired alignment of the thrust vector. For this reason, the principal rotation vector of the third rotation, $\hat{\boldsymbol{e}}_\theta$, is defined as:

$$\hat{\boldsymbol{e}}_\theta = \frac{\boldsymbol{b}}{\|\boldsymbol{b}\|}. \tag{17}$$

The unknown variable in this problem is the principal rotation angle θ. Let us define the Classic Rodrigues Parameter (CRP) set, or Gibb's vector [32]:

$$\boldsymbol{q} = \hat{\boldsymbol{e}}_\theta \tan\left(\frac{\theta}{2}\right) \tag{18}$$

from which the third DCM is expressed as:

$$[\mathcal{D}_3\mathcal{D}_2] = \frac{\left((1 - \boldsymbol{q}^T\boldsymbol{q})[\boldsymbol{I}_{3\times3}] + 2\boldsymbol{q}\boldsymbol{q}^T - 2[\tilde{\boldsymbol{q}}]\right)}{1 + \boldsymbol{q}^T\boldsymbol{q}} \tag{19}$$

where $[\boldsymbol{I}_{3\times3}]$ is the three-dimensional identity matrix and the tilde operator denotes the skew-symmetric cross-product matrix. The goal is to obtain a final DCM $[\mathcal{F}\mathcal{M}]$ such that:

$$[\mathcal{F}\mathcal{M}] = [\mathcal{D}_3\mathcal{M}] = [\mathcal{D}_3\mathcal{D}_2][\mathcal{D}_2\mathcal{D}_1][\mathcal{D}_1\mathcal{M}] \tag{20}$$

is of the same form as Equation (8). Defining the following known quantities component-wise:

$$\hat{\boldsymbol{e}}_\theta = \{e_1, e_2, e_3\}^T \qquad [\mathcal{D}_2\mathcal{M}] = \begin{bmatrix} d_{11} & d_{12} & d_{13} \\ d_{21} & d_{22} & d_{23} \\ d_{31} & d_{32} & d_{33} \end{bmatrix}, \tag{21}$$

carrying out the product $[\mathcal{D}_3\mathcal{M}] = [\mathcal{D}_3\mathcal{D}_2][\mathcal{D}_2\mathcal{M}]$ and equating the element $(2, 1)$ of $[\mathcal{D}_3\mathcal{M}]$ to zero to meet the rotational constraint, gives the following equation:

$$\frac{At^2 + Bt + C}{1 + t^2} = 0 \qquad \text{with} \qquad t = \tan\left(\frac{\theta}{2}\right) \tag{22}$$

where:

$$\begin{aligned} A &= 2(d_{21}e_2^2 + d_{11}e_1e_2 + d_{31}e_2e_3) - d_{21} \\ B &= 2(d_{31}e_1 - d_{11}e_3) \\ C &= d_{21}. \end{aligned} \tag{23}$$

Equation (22) has solutions when $\Delta = B^2 - 4AC \geq 0$. In such a case, it is:

$$t = \frac{-B \pm \sqrt{\Delta}}{2A} \tag{24}$$

which can be plugged back into Equation (18) and subsequently into Equation (19) to obtain $[\mathcal{D}_3\mathcal{D}_2]$. Finally, Equation (20) yields the rotation $[\mathcal{F}\mathcal{M}]$ that complies with all the requirements. Defining f_{ij} for $i, j = 1, 2, 3$ the elements of the $[\mathcal{F}\mathcal{M}]$ matrix, the tip and tilt gimbal reference angles ν_{R1} and ν_{R2} in Equation (8) are obtained as:

$$\nu_{R1} = \arctan\left(\frac{f_{23}}{f_{22}}\right) \qquad \nu_{R2} = \arctan\left(\frac{f_{31}}{f_{11}}\right). \tag{25}$$

Relatively to Equation (22), it is possible to prove that

$$\Delta = \|\hat{\boldsymbol{d}} \times \hat{\boldsymbol{e}}_\theta\|^2 - e_2^2 \qquad \text{with} \qquad \hat{\boldsymbol{d}} = \{d_{11}, d_{21}, d_{31}\}^T. \tag{26}$$

Therefore, it can not be proved that $\Delta \geq 0$ strictly. However, more insight is gained considering the physical interpretation of e_2 that appears in the Δ expression. This is the second component of the unit vector that defines the direction of the CM with respect to the mount frame origin M. In the geometry outlined in this paper, the system CM is primarily along the z axis, so for the case presented here, e_2^2 is small compared to the other quantities that appear in the expression of Δ. For spacecraft with very different geometries, it is possible to define a different principal rotation vector $\hat{\boldsymbol{\epsilon}} = \{\epsilon_1, \epsilon_2, \epsilon_3\}^T$ whose angular distance from $\hat{\boldsymbol{e}}_\theta$ is minimum and for which $\Delta(\hat{\boldsymbol{\epsilon}}) = 0$. Performing the third rotation about $\hat{\boldsymbol{\epsilon}}$ would yield a constraint-compliant platform rotation, while breaking the alignment with the CM by the minimum allowable amount. Such problem can be set up as a constrained maximization problem via Lagrange multipliers, maximizing the cost function:

$$F(\hat{\boldsymbol{\epsilon}}) = \hat{\boldsymbol{\epsilon}} \cdot \hat{\boldsymbol{e}}_\theta + \lambda_1(\epsilon_1^2 + \epsilon_2^2 + \epsilon_3^2 - 1) + \lambda_2(\|\hat{\boldsymbol{d}} \times \hat{\boldsymbol{\epsilon}}\|^2 - \epsilon_2^2). \tag{27}$$

While a closed-form solution is found for the Lagrange multipliers:

$$\lambda_1 = -\frac{\hat{\boldsymbol{\epsilon}} \cdot \hat{\boldsymbol{e}}_\theta}{2} \qquad \lambda_2 = \frac{\hat{\boldsymbol{d}} \cdot \hat{\boldsymbol{e}}_\theta - (\hat{\boldsymbol{\epsilon}} \cdot \hat{\boldsymbol{d}})(\hat{\boldsymbol{\epsilon}} \cdot \hat{\boldsymbol{e}}_\theta)}{2\epsilon_2 d_{22}}, \tag{28}$$

finding $\hat{\boldsymbol{\epsilon}}$ requires solving a system of 3 nonlinear equations for which no closed form solution is available.

4 Continuous Momentum Management via SEP Thruster

The previous section shows how, by means of three consecutive rigid body rotations, it is possible to align the thrust vector with a point C on the hub. This point C can coincide with the center of mass of the whole spacecraft: in such a case, the thrust does not produce any torque on the system. In contrast, it is possible to intentionally offset the thrust vector from the center of mass to leverage the resulting torque to perform momentum offloading.

4.1 Control Law Derivation with CM Knowledge

Let us define $\boldsymbol{H}_{\mathrm{RW}}$ as the total net momentum of the reaction wheels with respect to the hub:

$$\boldsymbol{H}_{\mathrm{RW}} = \sum_{j=1}^{4} J_{\mathrm{W}} \Omega_j \hat{\boldsymbol{u}}_j, \tag{29}$$

where $\hat{\boldsymbol{u}}_j$ is the spin axis of each individual RW. To compensate for the action of external torques, it is therefore necessary to point the thruster at an offset that results in a thrust torque that opposes the current RW net momentum. Let us define such an offset vector $\boldsymbol{d}$, and the resulting thruster torque $\boldsymbol{L}_{\mathrm{thr}}$. Over an infinitesimal time interval $\Delta\tau$ it is:

$$-\Delta\boldsymbol{H} = \boldsymbol{L}_{\mathrm{thr}} \Delta\tau = \boldsymbol{d} \times \boldsymbol{t} \Delta\tau, \tag{30}$$

where $\Delta\boldsymbol{H}$ is the amount of momentum to be offloaded. Generally, this can be the amount of wheel momentum that exceeds a certain threshold, to ensure that wheel speeds are driven to safe nonzero operational values. Conversely, it can coincide with the total momentum on the wheels ($\Delta\boldsymbol{H} = \boldsymbol{H}_{\mathrm{RW}}$) when the goal is to drive the wheel speeds to zero. To obtain $\boldsymbol{d}$, both sides of the previous equation are cross-multiplied by $\boldsymbol{t}$. Expanding the double cross product and choosing $\boldsymbol{d}$ such that $\boldsymbol{d} \perp \boldsymbol{t}$ gives:

$$\begin{aligned} -\boldsymbol{t} \times \Delta\boldsymbol{H} &= \boldsymbol{t} \times (\boldsymbol{d} \times \boldsymbol{t}) \Delta\tau \\ &= [t^2 \boldsymbol{d} - (\boldsymbol{t} \cdot \boldsymbol{d}) \boldsymbol{t}] \Delta\tau \\ &= t^2 \boldsymbol{d} \Delta\tau \end{aligned} \tag{31}$$

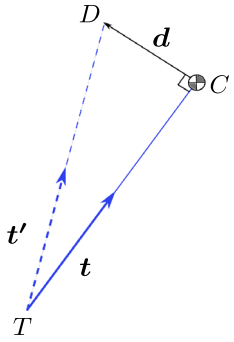

Fig. 5 Center of mass offset

which ultimately yields the control law:

$$\boldsymbol{d} = -\frac{\kappa}{t^2}(\boldsymbol{t} \times \boldsymbol{H}_{\mathrm{RW}}) \tag{32}$$

where $\kappa = 1/\Delta\tau$ [Hz] is a proportional control gain. In this paper, the reaction wheels are operated from an initial zero-spin configuration and with the intention of using this control law to drive their transient speeds back to zero. The reason for this choice is that it allows for an easier interpretation of the results, where nonzero final wheel speeds are the effect of external torques acting on the system. Conversely, final wheels speeds that approach zero indicate the successful application of the control law. For this reason, Equation (32) is derived with $\Delta\boldsymbol{H} = \boldsymbol{H}_{\mathrm{RW}}$, coherently with the authors' choice to facilitate the interpretation of numerical results.

With respect to Figure 5, $\boldsymbol{t}$ is the zero-torque thrust vector, or the thrust vector when the thruster is aligned with the system CM. $\boldsymbol{t}'$, on the other hand, is the thrust vector obtained aligning the thruster at the offset computed in Equation (32). The resulting thruster torque is:

$$\boldsymbol{L}_{\mathrm{thr}} = \boldsymbol{d} \times \boldsymbol{t}' = \frac{\kappa}{t^2}\boldsymbol{t}' \times (\boldsymbol{t} \times \boldsymbol{H}_{\mathrm{RW}}) \tag{33}$$

which is an underactuated control torque. As the result of a cross product, no control can be delivered along the direction of $\boldsymbol{t}$, which means that components of wheel momentum along such direction will remain unaffected. Another interesting fact about Equation (33) is that the resulting thruster torque is implicitly independent of the thrust magnitude t, as it depends only on the wheel momentum and control gain κ.

To better characterize Equation (32) and (33) from an implementation perspective, let us recall the description of the thruster-platform assembly given in Section 3, where the coordinates of the thrust vector $\boldsymbol{t}$ are assumed known in the platform frame $\mathcal{F}$, and its coordinates in the mount and body frames $\mathcal{M}$ and $\mathcal{B}$ are pending knowledge of the angle of the platform gimbal, according to Equation (8). To know the coordinates of $\boldsymbol{t}$ in the $\mathcal{M}$ and $\mathcal{B}$ frames, it is necessary to compute the tip and tilt angles ν_{R1} and ν_{R2} that corresponding to the rigid body rotation that aligns the thruster with a desired point in the body frame, as outlined in Section 3. For $\boldsymbol{t}$, the alignment is with the center of mass C, or the best estimate thereof at the given time. From the knowledge of ${}^{\mathcal{B}}\hat{\boldsymbol{t}}$ and

${}^{\mathcal{B}}\hat{\boldsymbol{H}}_{\mathrm{RW}}$ it is possible to define point D through the offset vector ${}^{\mathcal{B}}\hat{\boldsymbol{d}}$, as summarized by Figure 5. Point D becomes the new target fot the platform guidance algorithm, whose outputs, the new gimbal angles ν'_{R1} and ν'_{R2} allow to point the thruster-platform assembly along ${}^{\mathcal{B}}\hat{\boldsymbol{t}}'$.

4.2 Stability Analysis

It is possible to show that the control law for thruster pointing in Equation (32) can, under certain assumptions, drive the net wheel momentum in Equation (29) to zero. This is done applying Lyapunov's direct method, defining the candidate Lyapunov function:

$$V(\boldsymbol{H}) = \frac{\boldsymbol{H}\cdot\boldsymbol{H}}{2} = \frac{H^2}{2} \tag{34}$$

which is positive definite. Let us assume simplified spacecraft dynamics, where the spacecraft hub is not tumbling ($\boldsymbol{\omega}_{\mathcal{B}/\mathcal{N}} = 0$) and the only external torque acting on the system is the thruster torque in Equation (33). Let us also assume a very fast response from the RWs, such that all thruster torque is stored in the form of RW net momentum, i.e. $\dot{\boldsymbol{H}} = \dot{\boldsymbol{H}}_{\mathrm{RW}} = \boldsymbol{L}_{\mathrm{thr}}$. Under these assumptions, the derivative of the Lyapunov function becomes:

$$\begin{aligned}\dot{V}(\boldsymbol{H}) = \boldsymbol{H}\cdot\dot{\boldsymbol{H}} &= \frac{\kappa}{t^2}\boldsymbol{H}\cdot\left[\boldsymbol{t}'\times(\boldsymbol{t}\times\boldsymbol{H})\right]\\ &= \frac{\kappa}{t^2}\boldsymbol{H}\cdot\left[(\boldsymbol{t}'\cdot\boldsymbol{H})\boldsymbol{t} - (\boldsymbol{t}\cdot\boldsymbol{t}')\boldsymbol{H}\right]\\ &= -\kappa H^2\left[(\hat{\boldsymbol{t}}\cdot\hat{\boldsymbol{t}}') - (\hat{\boldsymbol{t}}\cdot\hat{\boldsymbol{H}})(\hat{\boldsymbol{t}}'\cdot\hat{\boldsymbol{H}})\right].\end{aligned} \tag{35}$$

Proving that Equation (35) is negative semi-definite would ensure that the system is stable in the sense of Lyapunov [33]. For this purpose, let us define $\hat{\boldsymbol{t}} = a\hat{\boldsymbol{H}} + \boldsymbol{u}$ and $\hat{\boldsymbol{t}}' = b\hat{\boldsymbol{H}} + \boldsymbol{v}$, such that $\hat{\boldsymbol{H}}\cdot\boldsymbol{u} = 0$ and $\hat{\boldsymbol{H}}\cdot\boldsymbol{v} = 0$, that is, the decomposition of $\hat{\boldsymbol{t}}$ and $\hat{\boldsymbol{t}}'$ in their components parallel and perpendicular to $\hat{\boldsymbol{H}}$. Equation (35) becomes:

$$\dot{V}(\boldsymbol{H}) = -\kappa H^2\left[ab + \boldsymbol{u}\cdot\boldsymbol{v} - ab\right] = -\kappa H^2(\boldsymbol{u}\cdot\boldsymbol{v}). \tag{36}$$

The Lyapunov derivative is therefore negative definite when $\boldsymbol{u}\cdot\boldsymbol{v} > 0$, that is, when the components of $\hat{\boldsymbol{t}}$ and $\hat{\boldsymbol{t}}'$ orthogonal to $\hat{\boldsymbol{H}}$ are non-zero and for an acute angle with one-another.

From a design perspective, it is desirable to choose a small κ to avoid chattering about the zero-torque direction, and also to avoid computing too large an offset $\boldsymbol{d}$ that cannot be realized by the thruster gimbals. A small κ also means that the offset $\boldsymbol{d}$ results in a small variation of the thrust vector from the zero-torque direction, which satisfies the condition $\boldsymbol{u}\cdot\boldsymbol{v} > 0$. In the limit for κ so small that the thrust direction vector can be considered almost unchanged from the zero-torque configuration ($\hat{\boldsymbol{t}}' \approx \hat{\boldsymbol{t}}$), the following simplification can be made:

$$\boldsymbol{L}_{\text{thr}} \approx \frac{\kappa}{t^2}\boldsymbol{t} \times (\boldsymbol{t} \times \boldsymbol{H}) \tag{37}$$

and the Lyapunov derivative becomes:

$$\dot{V}(\boldsymbol{H}) = -\kappa H^2 \left[1 - (\hat{\boldsymbol{t}} \cdot \hat{\boldsymbol{H}})^2\right]. \tag{38}$$

$\dot{V}(\boldsymbol{H})$ is therefore globally negative semi-definite, making the system always stable, and negative definite if $\boldsymbol{t}$ has no components along $\boldsymbol{H}_{\text{RW}}$. In practical terms, this control law is globally stable, and asymptotically stable for the components of the net wheel momentum $\boldsymbol{H}_{\text{RW}}$ orthogonal to the thrust vector. A steady state is reached when the the angular momentum is parallel to the thrust direction vector.

4.3 Control Law Derivation without CM Knowledge

In the previous derivation the location of the system CM was considered known. More generally, the CM location can be known within a certain accuracy, and it changes significantly over the course of a multi-year mission. For the purpose of using the SEP thruster for momentum management, a wrong CM estimate can lead to an inaccurate steady state thruster pointing that results in parasitic torques on the system, contributing to the growth of net RW momentum over time. For this reason, Equation (32) can be enhanced with the addition of an integral term as follows:

$$\boldsymbol{d} = -\frac{\boldsymbol{t}}{t^2} \times (\kappa \boldsymbol{H} + \kappa_I \boldsymbol{H}_I) \tag{39}$$

where:

$$\boldsymbol{H}_I = \int_0^t \boldsymbol{H} \mathrm{d}\tau. \tag{40}$$

and the units of κ_I are Hz^2. The subscript RW in $\boldsymbol{H}$ is removed from now on for ease of notation. When the net momentum grows over time, the integral feedback term corrects the offset $\boldsymbol{d}$ to align the thruster with the real CM location. The stability analysis can be performed defining a new Lyapunov function:

$$V(\boldsymbol{H}, \boldsymbol{H}_I) = \frac{H^2}{2} + \kappa_I \frac{H_I^2}{2} \tag{41}$$

which is positive definite. The derivative is:

$$\begin{aligned} \dot{V}(\boldsymbol{H}, \boldsymbol{H}_I) &= \boldsymbol{H} \cdot \left(\dot{\boldsymbol{H}} + \kappa_I \boldsymbol{H}_I\right) \\ &= \boldsymbol{H} \cdot \left\{ \frac{\boldsymbol{t}}{t^2} \times [\boldsymbol{t} \times (\kappa \boldsymbol{H} + \kappa_I \boldsymbol{H}_I)] + k_I \boldsymbol{H}_I \right\} = -\kappa H^2 \end{aligned} \tag{42}$$

where Equation (39) is used in the torque expression and negligible thruster direction variations ($\hat{\boldsymbol{t}}' \approx \hat{\boldsymbol{t}}$) are considered. The final result of Equation (42) is obtained with

$\boldsymbol{t}\cdot\boldsymbol{H}=0$, i.e., disregarding momentum components along the local thrust vector. What this means is that the stability claims made in this section only apply to the angular momentum components orthogonal to the thrust vector. The result of Equation (42) only proves that the derivative of the Lyapunov function is negative semidefinite, because there is no trace of $\boldsymbol{H}_I$ in the expression. This guarantees stability in the sense of Lyapunov, but to prove asymptotic stability, higher-order derivatives must be computed and evaluated on the set in which $\dot{V}(\boldsymbol{H},\boldsymbol{H}_I)=0$ [34], which is $\boldsymbol{H}=0$. For the second-order derivative it is:

$$\begin{aligned}\ddot{V}(\boldsymbol{H},\boldsymbol{H}_I) &= -2\kappa\boldsymbol{H}\cdot\dot{\boldsymbol{H}} = -2\kappa\boldsymbol{H}\cdot\left\{\frac{\boldsymbol{t}}{t^2}\times[\boldsymbol{t}\times(\kappa\boldsymbol{H}+\kappa_I\boldsymbol{H}_I)]\right\}\\ &= 2\kappa\boldsymbol{H}\cdot(\kappa\boldsymbol{H}+\kappa_I\boldsymbol{H}_I)\end{aligned} \tag{43}$$

which is once again obtained with $\boldsymbol{t}\cdot\boldsymbol{H}=0$. The Lyapunov stability of the system implies that $\boldsymbol{H}$ and $\boldsymbol{H}_I$ are bounded, therefore if follows that $\ddot{V}_{\boldsymbol{H}=0}=0$. The third derivative gives:

$$\begin{aligned}\dddot{V}(\boldsymbol{H},\boldsymbol{H}_I) &= 2\kappa\dot{\boldsymbol{H}}\cdot(\kappa\boldsymbol{H}+\kappa_I\boldsymbol{H}_I)+2\kappa\boldsymbol{H}\cdot\left(\kappa\dot{\boldsymbol{H}}+\kappa_I\boldsymbol{H}\right)\\ &= 2\kappa\,(2\kappa\boldsymbol{H}+\kappa_I\boldsymbol{H}_I)\cdot\left\{\frac{\boldsymbol{t}}{t^2}\times[\boldsymbol{t}\times(\kappa\boldsymbol{H}+\kappa_I\boldsymbol{H}_I)]+k_I\boldsymbol{H}_I\right\}+2\kappa\kappa_I H^2\\ &= 2(\kappa_I-2\kappa^2)\kappa H^2-6\kappa^2\kappa_I\boldsymbol{H}\cdot\boldsymbol{H}_I-2\kappa\kappa_I^2H_I^2\left[1-(\hat{\boldsymbol{t}}\cdot\hat{\boldsymbol{H}}_I)^2\right]\end{aligned} \tag{44}$$

which evaluated on the set $\boldsymbol{H}=0$ gives:

$$\dddot{V}_{\boldsymbol{H}=0} = -2\kappa\kappa_I^2H_I^2\left[1-(\hat{\boldsymbol{t}}\cdot\hat{\boldsymbol{H}}_I)^2\right]. \tag{45}$$

This result is analogous to that of Equation (38), where the function is negative definite except for the case in which the integral of the net momentum is aligned with the thrust vector. With this caveat, the third derivative being negative definite on the set $\boldsymbol{H}=0$ proves that the control law in Equation (39) is indeed asymptotically stabilizing for the components of reaction wheel angular momentum orthogonal to the thrust vector.

5 Continuous Momentum Management via Rotating Solar Arrays

Section 4 shows how it is possible to use a gimbaled SEP thruster to continuously offload momentum along two spacecraft body axes, but also highlights the underactuated character of this technique, as a result of which momentum buildup along one axis remains uncontrolled. This section aims to take advantage of the rotating solar arrays to leverage the SRP torque and perform momentum offloading along the axis that cannot be controlled by the SEP thruster. It is important to note that this strategy might not be suitable to all missions, as it requires to depart from the condition of optimal power generation: such condition is met when the power-generating surface of the arrays is orthogonal to incoming sunlight, or as close to it as possible. However,

during segments of a mission in which the SEP thruster is not active, it is reasonable to assume that the spacecraft does not need to operate at full power. Similarly, when the spacecraft flies closer to the inner regions of the Solar System, more power is generated as a consequence of the proximity to the Sun, so a suboptimal array configuration might be sufficient.

5.1 Symmetric, Fully-absorbent Solar Arrays

This analysis applies to a pair of symmetric solar arrays that can rotate about antiparallel, body-fixed spacecraft axes. The spacecraft attitude is considered given, with the body frame $\mathcal{B}$ aligned with the reference frame $\mathcal{R}$. The aim is to articulate the arrays differentially in order to result in a net SRP torque in the opposite direction to RW net momentum. This analysis considers only the SRP acting on the arrays, and it neglects secondary effects such as the SRP on the spacecraft hub or secondary reflections of photons. The arrays are modeled as two-dimensional panels with negligible thickness, and their rigid motion is described by frames $\mathcal{A}$ as illustrated in Figure 3. With respect to each array frame, the SRP force is modeled according to the formulation provided by Rodriguez et al. [35], but for the purpose of the control law defined in this subsection, the arrays are considered fully absorbent. The SRP force then simplifies to:

$$\boldsymbol{F}_{\text{SRP,abs}} = -PA\left(\hat{\boldsymbol{s}} \cdot \hat{\boldsymbol{a}}_2\right)\hat{\boldsymbol{s}}. \tag{46}$$

where A is the surface area of each array, P the solar radiation pressure at that distance from the Sun, and $\hat{\boldsymbol{s}}$ points towards the Sun. In reality, solar arrays are not fully absorbent, but absorption coefficients for modern solar cells are usually around $\lambda \geq 0.75$ [36]. In practical terms, this means that only a small fraction of the incoming light is reflected and diffusely scattered, resulting in only a minor contribution of SRP force orthogonal to the Sun direction. It is easy to show that for $\hat{\boldsymbol{s}} \cdot \hat{\boldsymbol{a}}_2 = \cos\theta = 1$ the force is maximum, while it vanishes for $\hat{\boldsymbol{s}} \perp \hat{\boldsymbol{a}}_2$. The goal of this analysis is to rotate the array whose resulting SRP torque feeds positively into the net RW momentum. For this purpose, let us consider small array deflection angles θ with respect to the Sun direction. In the following, the subscripts $\pm$ are used to denote positive and negative contributions to the axis uncontrolled by the SEP thruster. The net SRP torque acting on the arrays can be expressed as:

$$\begin{aligned}\boldsymbol{L}_{\text{SRP,net}} &= \boldsymbol{r}_{O/C,+} \times \boldsymbol{F}_{\text{SRP},+} + \boldsymbol{r}_{O/C,-} \times \boldsymbol{F}_{\text{SRP},-} \\ &= -PA(\cos\theta_+ - \cos\theta_-)\left(\boldsymbol{r}_{O/C} \times \hat{\boldsymbol{s}}\right)\end{aligned} \tag{47}$$

where $\boldsymbol{r}_{O/C,i}$ are the distance between the system CM and the center of pressure of each array, which for symmetric geometries correspond to the geometric centers, and from symmetry of the solar arrays it is $\boldsymbol{r}_{O/C} = \boldsymbol{r}_{O/C,+} = -\boldsymbol{r}_{O/C,-}$. Let us define the quantities:

$$\eta_i = -\left(\boldsymbol{r}_{O/C,i} \times \hat{\boldsymbol{s}}\right) \cdot \boldsymbol{H}_{\text{RW}}, \tag{48}$$

which are proportional to the net RW momentum as defined in Equation (29). From these, it is possible to consider the following control law for the deflection angles of

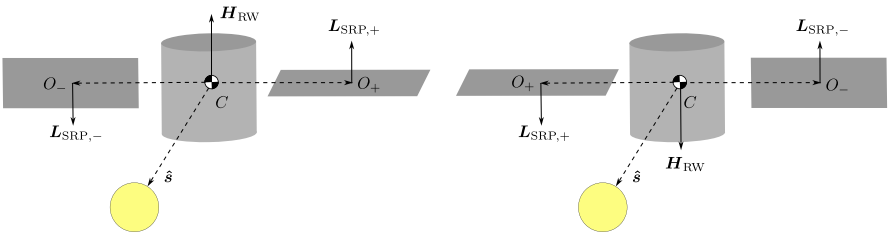

(a) Positive net momentum (b) Negative net momentum

Fig. 6 Array orientation for different net momentum configurations

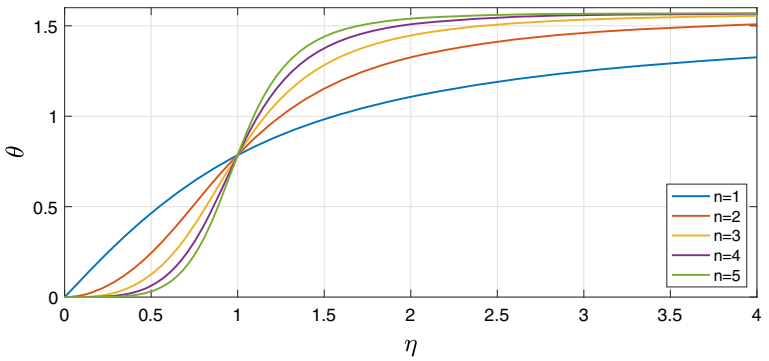

Fig. 7 Control law in Equation (49) with $\xi = 1$ and $\Theta = 1$

the arrays:

$$\theta_i = \begin{cases} \Theta \arctan\left(\xi \eta_i^n\right) & \text{if } \eta_i > 0 \\ 0 & \text{if } \eta_i \leq 0 \end{cases}. \tag{49}$$

The control law in Equation (49) ensures that the array that produces a negative feedback SRP torque (η_-) is not deflected, but rather left orthogonal to the incoming sunlight to maximize the resulting SRP torque. In contrast, the array that produces a positive feedback torque (η_+) is deflected proportionally to the net RW momentum to reduce the contribution of such a positive feedback, as illustrated in Figure 6. The arctangent function and the factor Θ are used to limit the deflection angle to the $[-\frac{\Theta\pi}{2}, \frac{\Theta\pi}{2}]$ domain, where the introduction of $0 < \Theta \leq 1$ is intended to avoid edge-on configurations where one array would produce no power. The factor ξ is a control gain, while the exponent n is introduced because, for $n > 1$, it is possible to obtain a deadband in the control law that has the benefit of limiting the chattering around $\theta = 0$, as shown in Figure 7.

5.2 Stability Analysis

To prove the stability of the control law in Equation (49), it is useful to start from the Taylor series expansion of $\cos(\theta(\eta))$ for small deflection angles. This gives:

$$\cos(\theta(\eta)) = \cos\left(\Theta \arctan\left(\xi \eta^n\right)\right) \approx 1 - \frac{\Theta^2 \xi^2 \eta^{2n}}{2} + o(\eta^{2n+1}). \tag{50}$$

Plugging this result back into the net SRP torque in Equation (47) allows to compute a simplified dynamics model, with the SPR torque as that the only torque acting on the system:

$$\dot{\boldsymbol{H}} = \boldsymbol{L}_{\text{SRP,net}} = -PA\left(1 - \frac{\Theta^2 \xi^2 \eta_+^{2n}}{2} - 1\right)\left(\boldsymbol{r}_{O/C} \times \hat{\boldsymbol{s}}\right) = \frac{1}{2} PA\Theta^2 \xi^2 \eta_+^{2n}\left(\boldsymbol{r}_{O/C} \times \hat{\boldsymbol{s}}\right). \tag{51}$$

Considering the positive definite candidate Lyapunov function $V(\boldsymbol{H}) = H^2$ and under the same assumption of fast RW response as in Section 4, for which $\dot{\boldsymbol{H}} = \dot{\boldsymbol{H}}_{\text{RW}} = \boldsymbol{L}_{\text{SRP,net}}$, the Lyapunov derivative is:

$$\dot{V}(\boldsymbol{H}) = PA\Theta^2 \xi^2 \eta_+^{2n}\left(\boldsymbol{r}_{O/C} \times \hat{\boldsymbol{s}}\right) \cdot \boldsymbol{H}_{\text{RW}} = -PA\Theta^2 \xi^2 \eta_+^{2n+1}. \tag{52}$$

Per hypothesis, the only array to deflect is the one whose SRP torque feeds positively into the net momentum, i.e. $\eta_+ = -\left(\boldsymbol{r}_{O/C,+} \times \hat{\boldsymbol{s}}\right) \cdot \boldsymbol{H}_{\text{RW}} > 0$. Under such a hypothesis, the Lyapunov derivative is negative definite, and the control law asymptotically stabilizing. The case may exist where the vectors $\boldsymbol{r}_{O/C}$, $\hat{\boldsymbol{s}}$, and $\boldsymbol{H}_{\text{RW}}$ are colinear. If the net RW is parallel to the Sun direction, for instance, it is $\eta_+ = \eta_- = 0$, in which case the Lyapunov derivative becomes identically zero. In this case, analogous stability considerations can be made as in Section 4: this control method is locally asymptotically stable for the components of momentum that are not orthogonal to the cross product $\boldsymbol{r}_{O/C} \times \hat{\boldsymbol{s}}$.

6 Center of Mass Estimation

This section is motivated by the need to perform continuous CM estimation over the extended periods of time during which the electric thruster is firing, without interrupting the nominal course of operations to perform calibration slew maneuvers to compute the exact location of the CM. Therefore, the aim for this section is to remove the assumption that the location of the system's CM is known, and rather estimate the CM location based on measurements of the system's states when the hub converges to the desired reference frame.

6.1 Traditional approaches

Traditional CM estimation algorithms, such as that described by Bergmann et al. [19], rely on accelerometers mounted on the spacecraft hub. The measurement model is given by the relative acceleration theorem:

$$\boldsymbol{a} = \boldsymbol{a}_{CM} + \dot{\boldsymbol{\omega}}_{\mathcal{B}/\mathcal{N}} \times \boldsymbol{r} + \boldsymbol{\omega}_{\mathcal{B}/\mathcal{N}} \times (\boldsymbol{\omega}_{\mathcal{B}/\mathcal{N}} \times \boldsymbol{r}) + 2\boldsymbol{\omega}_{\mathcal{B}/\mathcal{N}} \times \dot{\boldsymbol{r}} \tag{53}$$

where $\boldsymbol{a}$ is the measured quantity, and $\boldsymbol{r}$ is the location of the center of mass to be estimated. Because the CM location does not vary quickly over time ($\dot{\boldsymbol{r}} = 0$), and the system is not subject to external forces ($\boldsymbol{a}_{CM} = 0$), the above equation is simplified to the linear model:

$$\boldsymbol{a} = [\boldsymbol{H}(\boldsymbol{\omega}_{\mathcal{B}/\mathcal{N}}, \dot{\boldsymbol{\omega}}_{\mathcal{B}/\mathcal{N}})]\boldsymbol{r} \tag{54}$$

where the angular rates and accelerations of the hub are obtained from IMU measurements. These arguments, however, are not valid in the case of a thrust system such as the one considered in this paper. Because the external force acting on the system is not zero, the acceleration of the CM cannot be neglected:

$$\boldsymbol{a}_{CM} = \boldsymbol{t}/m \tag{55}$$

where $\boldsymbol{t}$ is the thrust vector, and m is the mass of the system, which are both subject to uncertainty. Moreover, because the thruster must be aligned with a certain inertial direction, the angular rates and accelerations of the hub are typically zero, except during transient control responses. This makes it such that the linear model in Equation (54) reduces to a matrix whose entries are all close to zero, thus making the estimation problem weakly observable during nominal pointing operations that do not involve ad-hoc maneuvers to generate a transient response.

6.2 Steady-state reference tracking

It is interesting to take a closer look at the control law Equation (1) when the system converges to the desired reference frame $\mathcal{R}$. Because the reference is in first approximation static, to ensure inertial pointing of the thruster, it is $\boldsymbol{\omega}_{\mathcal{R}/\mathcal{N}} = \dot{\boldsymbol{\omega}}_{\mathcal{R}/\mathcal{N}} = 0$. Under these assumptions, Equation (1) is reduced to a regulator control law:

$$\boldsymbol{u} = -K\boldsymbol{\sigma}_{\mathcal{B}/\mathcal{N}} - P\boldsymbol{\omega}_{\mathcal{B}/\mathcal{N}} - PK_I\boldsymbol{z} \quad \text{with} \quad \boldsymbol{z} = K\int_{t_0}^{t} \boldsymbol{\sigma}_{\mathcal{B}/\mathcal{R}}\mathrm{d}t + [\boldsymbol{J}_{\mathrm{tot},C}]\boldsymbol{\omega}_{\mathcal{B}/\mathcal{N}} \tag{56}$$

where the gyroscopic term $\boldsymbol{\omega}_{\mathcal{B}/\mathcal{N}} \times \left([\boldsymbol{J}_{\mathrm{tot},C}]\boldsymbol{\omega}_{\mathcal{B}/\mathcal{N}} + [\boldsymbol{G}_s]\boldsymbol{h}_s\right)$ is dropped without affecting the asymptotic stability properties of the control law [3], and the reference frame $\mathcal{R}$ is made coincide with the inertial frame $\mathcal{N}$, as it remains fixed in time. Additionally, once convergence to the reference frame is achieved, it holds true that $\boldsymbol{\sigma}_{\mathcal{B}/\mathcal{R}} \approx \boldsymbol{\omega}_{\mathcal{B}/\mathcal{R}} \approx 0$. When this steady-state condition is met, the control torque is further reduced to:

$$\boldsymbol{u}_{\text{ss}} = -PK_I\boldsymbol{z} = -PK_IK\int_{t_0}^{t}\boldsymbol{\sigma}_{\mathcal{B}/\mathcal{R}}\mathrm{d}t \tag{57}$$

where the control torque effectively coincides with the integral feedback term, and any dependence on the inertia of the system is lost. This means that, once steady state is achieved, the control torque required to stabilize the system is not affected by potential errors in the inertia tensor, which in contrast would only affect the transient response.

6.3 Measurement Model

The dynamics of the system when solar arrays and platform reach steady-state response are given in Equation (7). With respect to Figure 3, the thruster torque on the system can be modeled as:

$$\boldsymbol{L}_{\text{thr}} = -\boldsymbol{r}_{C/T}\times\boldsymbol{t} = [\tilde{\boldsymbol{t}}]\boldsymbol{r}_{C/T} \tag{58}$$

where point T is the thrust application point, and it is known, and point C is the location of the CM, which is to be estimated.

Taking into consideration Equation (7) (57) and (58), and considering the steady state where the system has converged to the reference frame, the following correlation can be highlighted between the integral feedback term and the thruster torque:

$$\boldsymbol{Z} = [\tilde{\boldsymbol{t}}]\boldsymbol{r}_{C/T} \tag{59}$$

where $\boldsymbol{Z} = PK_I\boldsymbol{z}$. Equation (59) constitutes a linear measurement model for the CM location, where the thrust direction vector $\boldsymbol{t}$ is, in first approximation, known, and the integral term $\boldsymbol{Z}$ is extracted from the flight software code segment that computes the torque delivered to the system by the reaction wheels at steady state. Because the platform orientation changes with time, so does the thrust application point T. For this reason, the measurement model can be better reformulated introducing point B, the origin of the body frame $\mathcal{B}$, whose coordinates are known and do not change over time. The problem is therefore formulated in terms of the position of the CM with respect to point B:

$$\boldsymbol{Z} + [\tilde{\boldsymbol{t}}]\boldsymbol{r}_{T/B} = [\tilde{\boldsymbol{t}}]\boldsymbol{r}_{C/B} \tag{60}$$

where $\boldsymbol{r}_{T/B}$ is the location of point T with respect to point B, and it is known accurately thanks to the reliable knowledge of the gimbal angles of the platform.

The main source of uncertainty is the thrust vector $\boldsymbol{t}$. Although the mapping between the thruster-platform frame $\mathcal{F}$ and the body frame $\mathcal{B}$ is accurately known, the knowledge of the thrust vector in $\mathcal{B}$-frame coordinates ${}^{\mathcal{B}}\boldsymbol{t}$ ultimately depends on how accurately the thruster's performance is known in its own frame $\mathcal{F}$. This means that if the thruster is misaligned with respect to the nominal direction, or if the magnitude of the thrust vector is off-nominal, the reliability of the measurement model is degraded.

6.4 Observability

Based on the considerations made in the previous subsection, it is possible to define the following system:

$$\begin{cases} \dot{\boldsymbol{x}} = [\boldsymbol{A}]\boldsymbol{x} \\ \boldsymbol{y} = [\boldsymbol{C}]\boldsymbol{x} \end{cases} \tag{61}$$

where $\boldsymbol{x} = \boldsymbol{r}_{C/B}$ is the quantity to be estimated, $\boldsymbol{y} = \boldsymbol{Z} + [\tilde{\boldsymbol{t}}]\boldsymbol{r}_{T/B}$ constitutes the measurement, and $[\boldsymbol{C}] = [\tilde{\boldsymbol{t}}]$ the linear model. With the CM location only varying significantly over large time scales, primarily due to propellant depletion, it is $[\boldsymbol{A}] = 0_{3\times3}$. Analyzing the observability for a static configuration, i.e., a case in which the platform is not moving with respect to the hub, gives the following observability matrix [37]:

$$[\mathcal{O}] = \begin{bmatrix} [\boldsymbol{C}] \\ [\boldsymbol{C}][\boldsymbol{A}] \\ \vdots \\ [\boldsymbol{C}][\boldsymbol{A}]^{n-1} \end{bmatrix} = [\tilde{\boldsymbol{t}}]. \tag{62}$$

Because $[\tilde{\boldsymbol{t}}]$ is the skew-symmetric cross product matrix, it has rank 2. This means that, in such a static configuration, the CM location is not fully observable. This could be inferred from thinking about the problem from a physical standpoint: when no torque is acting on the system, i.e., $\boldsymbol{Z} = 0$, it means that the thruster is being fired exactly through the system's CM. The exact position of the CM remains unknown as it could lie anywhere along the thrust line.

However, the thrust vector does not remain constant in body-frame coordinates when the platform is actuated to perform momentum management. As a result, the measurement model is not static, but rather time-varying. In such case, the general observability matrix is defined as [38]:

$$[\mathcal{O}] = \begin{bmatrix} [\boldsymbol{C}](t) \\ \frac{\mathrm{d}}{\mathrm{d}t}[\boldsymbol{C}](t) \\ \vdots \\ \frac{\mathrm{d}^{n-1}}{\mathrm{d}t^{n-1}}[\boldsymbol{C}](t) \end{bmatrix}. \tag{63}$$

What this means in practical terms is that if the platform is held at a constant configuration, the problem is not fully observable. However, articulating the platform and taking measurements from different thruster-platform configurations makes the problem fully observable even when the CM location has no dynamics.

6.5 Recursive Least-Squares Algorithm

The recursive least-squares (LS) algorithm implemented to estimate the location of the CM, effectively, coincides with the correction step of a Kalman filter. In other words,

the algorithm is equivalent to a Kalman filter where the state has no dynamics, and therefore there is no prediction.

At every n-th measurement update, the following quantities are given:

- $\epsilon_n = \sqrt{|\boldsymbol{\sigma}_{\mathcal{B}/\mathcal{R}}|^2 + |\boldsymbol{\omega}_{\mathcal{B}/\mathcal{R}}|^2}$: convergence error
- $[\boldsymbol{C}_n] = [\tilde{\boldsymbol{t}}]$: linear model
- $\boldsymbol{y}_n = \boldsymbol{Z} + [\tilde{\boldsymbol{t}}]\boldsymbol{r}_{T/B}$
- $[\boldsymbol{K}_n]$: optimal gain
- $\boldsymbol{x}_n = \boldsymbol{r}_{C/B}$: CM location estimate
- $[\boldsymbol{P}_n]$: covariance of the state estimate.

The equations that define how to update each quantity at every step are, once again, those of the correction step in a regular Kalman filter [37]:

$$[\boldsymbol{K}_n] = [\boldsymbol{P}_n][\boldsymbol{C}_n]^T \left([\boldsymbol{C}_n][\boldsymbol{P}_n][\boldsymbol{C}_n]^T + [\boldsymbol{R}]\right)^{-1} \tag{64}$$

$$\boldsymbol{x}_{n+1} = \boldsymbol{x}_n + [\boldsymbol{K}_n]\left(\boldsymbol{y}_n - [\boldsymbol{C}_n]\boldsymbol{x}_n\right) \tag{65}$$

$$\left[\boldsymbol{P}_{n+1}\right] = \left([\boldsymbol{I}_{3\times 3}] - [\boldsymbol{K}_n][\boldsymbol{C}_n]\right)[\boldsymbol{P}_n]. \tag{66}$$

$[\boldsymbol{R}]$ is the measurement noise covariance, and it is constant for every measurement. Because the integral feedback torque is not a conventional measurement, defining the measurement noise is difficult. In this work, it is modeled as the variance of the integral feedback torque after the system has reached steady state according to the convergence error threshold. It is also interesting to consider the case where the platform gimbal angles are themselves affected by measurement noise: this affects the mapping $[FB]$ between the platform frame and body frame, which results in an uncertain estimate of the thrust vector. Because this quantity affects the measurement $\boldsymbol{y}_n$, its uncertainty should be combined with the uncertainty of the integral feedback term to produce $[\boldsymbol{R}]$. Uncertainty in the gimbal angles is not modeled in this work.

The convergence error ϵ_n is used as a measure of whether the system has reached steady state. If ϵ_n is large it means that the system has not converged to the reference; therefore the integral term $\boldsymbol{Z}$ is not representative of the thruster torque acting on the system. For this reason, measurements are only processed when the convergence error drops below a user-defined threshold $\epsilon_n < \bar{\epsilon}$, which is a tuning parameter for the algorithm and depends on the gains of the attitude control law and the dynamic properties of the system.

6.6 Biased Measurement

In the presence of unmodeled external perturbations such as SRP torque, a bias is implicitly added to the measurement model. This happens because the integral feedback control law in Equation (1) drives the spacecraft to the desired attitude regardless of the nature of the unmodeled perturbations, whether these are due to a thruster offset, SRP, or both. As a consequence, when a biased external perturbation acts on the system, a bias in the estimated CM location is observed even when coherent measurement noise $[\boldsymbol{R}]$ is added to the LS algorithm. This steady-state bias in the CM estimate can

be explained by factoring the SRP torque into the model, and introducing point C^*, which is the point whose coordinates are really estimated by the LS algorithm:

$$\begin{aligned} \boldsymbol{Z} &= [\tilde{\boldsymbol{t}}]\boldsymbol{r}_{C/T} + \boldsymbol{L}_{\text{ext}} \\ \boldsymbol{Z} &= [\tilde{\boldsymbol{t}}]\left(\boldsymbol{r}_{C/C^*} + \boldsymbol{r}_{C^*/B} + \boldsymbol{r}_{B/T}\right) + \boldsymbol{L}_{\text{ext}} \\ \boldsymbol{Z} + [\tilde{\boldsymbol{t}}]\left(\boldsymbol{r}_{T/B} + \boldsymbol{r}_{C^*/C}\right) - \boldsymbol{L}_{\text{ext}} &= [\tilde{\boldsymbol{t}}]\boldsymbol{r}_{C^*/B}. \end{aligned} \tag{67}$$

The LS algorithm proceeds by correcting the CM location via subsequent increments that are orthogonal to the current thrust vector. Convergence is reached when subsequent increments are zero, resulting in an estimated CM location along the thrust vector itself. Due to the stabilizing nature of the control law that actuates the platform, the thruster reaches a steady-state configuration in which the external torques acting on the system are neutralized by the thruster action, to maintain the net momentum on the wheels near zero. Consequently, at steady state and in the presence of external disturbances, the thruster is not aligned with the center of mass, but rather with point C^*. This ensures that the resulting thruster torque is opposite to the external torque, minus the component along the thrust direction, which cannot be compensated by the thruster:

$$\boldsymbol{L}_{\text{net}} = \boldsymbol{L}_{\text{ext}} - \left(\boldsymbol{L}_{\text{ext}} \cdot \hat{\boldsymbol{t}}\right)\hat{\boldsymbol{t}} + \boldsymbol{r}_{C^*/C} \times \boldsymbol{t} = 0. \tag{68}$$

Combining Equation (67) and (68) gives:

$$\underbrace{\boldsymbol{Z} + [\tilde{\boldsymbol{t}}]\boldsymbol{r}_{T/B} - \left(\boldsymbol{L}_{\text{ext}} \cdot \hat{\boldsymbol{t}}\right)\hat{\boldsymbol{t}}}_{\boldsymbol{y}} = [\tilde{\boldsymbol{t}}]\underbrace{\boldsymbol{r}_{C^*/B}}_{\boldsymbol{x}} \tag{69}$$

which constitutes the effective measurement model in the presence of external perturbations, where the estimated C^* is the location of the effective center of mass, or center of equilibrium, which constitutes the moment arm for the thrust vector that balances external torques. In the absence of these, Equation (69) coincides with Equation (60), and the result of the estimation is the actual CM location. The estimation bias error can be expressed by taking the cross product between $\boldsymbol{t}$ and Equation (68):

$$\begin{aligned} \boldsymbol{t} \times \left(\boldsymbol{L}_{\text{ext}} - \left(\boldsymbol{L}_{\text{ext}} \cdot \hat{\boldsymbol{t}}\right)\hat{\boldsymbol{t}} + \boldsymbol{r}_{C^*/C} \times \boldsymbol{t}\right) &= \boldsymbol{t} \times 0 \\ \boldsymbol{t} \times \boldsymbol{L}_{\text{ext}} + \boldsymbol{t} \times \left(\boldsymbol{r}_{C^*/C} \times \boldsymbol{t}\right) &= 0 \\ \boldsymbol{t} \times \boldsymbol{L}_{\text{ext}} + t^2\boldsymbol{r}_{C^*/C} - (\boldsymbol{t} \cdot \boldsymbol{r}_{C^*/C})\boldsymbol{t} &= 0 \\ \boldsymbol{r}_{C^*/C} &= -\frac{\boldsymbol{t} \times \boldsymbol{L}_{\text{ext}}}{t^2} + (\hat{\boldsymbol{t}} \cdot \boldsymbol{r}_{C^*/C})\hat{\boldsymbol{t}}. \end{aligned} \tag{70}$$

With respect to Figure 8, C^* could lie anywhere along the thrust line $\boldsymbol{t}$, resulting in the same thruster torque with respect to the real CM. From Equation (70) it is possible to observe that the bias has a component that is orthogonal to the thrust vector and one that is parallel. The orthogonal component is inversely proportional in magnitude to the thrust. The parallel component is a product of the low observability of the problem which, at steady state, causes a loss of accuracy in the CM estimate along the thrust vector.

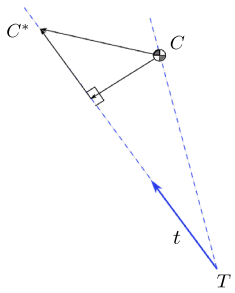

Fig. 8 Center of Mass bias

When fired through point C^*, the thruster compensates for two of the three components of the external torque, so long as this remains smaller or comparable in magnitude to the torque that the thruster can generate, and Equation (69) does not deviate too much from linearity.

It is worth mentioning that the stability of the system is reached despite a wrong CM estimate for the coupled algorithm suite of momentum management and CM estimation via gimbaled thruster presented in this paper. A wrong CM estimate can still present problems when used in combination with other actuators. For example, using cold gas thrusters for impulsive momentum dumping to control the residual momentum on the wheels would likely not work as desired, due to the wrong knowledge of the moment arms of the thruster application points with respect to the real CM. Similarly with other guidance, navigation and control algorithm that rely on the CM knowledge to operate properly. Particularly interesting is the case of a SEP thruster misfire, where the thrust output deviates from nominal expected behavior: in such a case, the unmodeled perturbation consists of the torque error with respect to nominal behavior. This error also in a bias in Equation (69), but ultimately does not prevent the system from converging to a stable configuration with the real thrust vector aligned with the effective CM. Although stable from an attitude standpoint, the error in thrust magnitude and/or direction would result in a deviation from the desired trajectory. Orbit determination in this case is required to estimate the entity of the thruster misfire and to compute a corrective thrust.

7 Simulation

7.1 Spacecraft properties

The spacecraft hub has a mass $m_{\text{hub}} = 2500$ kg and the following inertia tensor, expressed with respect to the principal body frame $\mathcal{B}$:

$$^{\mathcal{B}}[\boldsymbol{J}_{\text{hub}}] = \begin{bmatrix} 1725 & -5 & -12 \\ -5 & 5525 & 43 \\ -12 & 43 & 4810 \end{bmatrix} \text{ kg m}^2. \tag{71}$$

The location of the center of mass of the hub is ${}^{\mathcal{B}}\boldsymbol{r}_{C_{\text{hub}}/B} = \{0.008, -0.010, 1.214\}^T$ m with respect to the origin B of the body frame. The body frame is centered on the bottom surface of the spacecraft, modeled as a box of dimensions $1.80 \times 1.50 \times 2.86$ m.

The solar arrays are modeled as discs with a diameter of 7 m, whose center of mass is located at 3.75 m from the hinges, along the respective rotation axes ${}^{\mathcal{B}}\hat{\boldsymbol{a}}_1 = \{\pm 1, 0, 0\}^T$. The locations of the hinges in the hub are ${}^{\mathcal{B}}\boldsymbol{r}_{A/B} = \{\pm 0.75, 0, 0.45\}^T$ m. The mass of the solar arrays is $m_{\text{sa}} = 85$ kg and the inertia tensor is:

$$ {}^{\mathcal{S}}[\boldsymbol{J}_{\text{sa}}] = \begin{bmatrix} 260 & 0 & 0 \\ 0 & 260 & 0 \\ 0 & 0 & 520 \end{bmatrix} \text{ kg m}^2 \tag{72} $$

with respect to a principal frame $\mathcal{S}$ centered at the center of the disc, with the third axis $\hat{\boldsymbol{s}}_3$ orthogonal to the surface of the disc.

The four RWs have each a moment of inertia about the spin axis of $J_{\text{w}} = 0.16$ kg m^2. The thruster is assumed to fire continuously, with a specific impulse $I_{\text{sp}} = 1600$ s and a thrust output of $t = 0.27$ N. Under nominal conditions, the thrust is along the platform axis ${}^{\mathcal{F}}\hat{\boldsymbol{f}}_z = \{0, 0, 1\}^T$. The thruster output is affected by a parasitic swirl torque, which is the result of the rotational motion caused by the Lorentz forces acting on the thruster ejecta as they travel through the magnetic field of the thruster [39]. This swirl torque is modeled as a torque along the thrust direction vector, whose magnitude is proportional to the thrust magnitude, scaled by a factor of $\chi = 10^{-3}$ m:

$$ \boldsymbol{L}_{\text{swirl}} = \chi \boldsymbol{t}. \tag{73} $$

In the following simulations the swirl torque is generally neglected ($\chi = 0$), unless otherwise mentioned. In this mission scenario the RWs are the main actuator for attitude control, while absorbing external torques due to thruster offsets/misfires, and SRP. While their objective is to maintain the desired pointing, this mission does not pose strict pointing requirements: the goal is rather to maintain the total spacecraft momentum within operational limits. For this reason, zero-crossing wheel dynamics are not modeled in this work, and wheel speeds are allowed to cross zero and switch signs. This is coherent with the momentum magagement strategy adopted in the EMA mission, where the inverted swirl torque polarity of the SEP thruster is used ad an additional control variable to perform momentum managment, and RW zero crossings happen every 7-day thrust window as a design choice [13]. Other missions scenarions where finer attitude pointing is the driving requirement should implement lower bounds on the wheel speeds to avoid non-linearities and reduced wheel performances around zero-speed crossings.

With respect to Figure 3, the mount frame $\mathcal{M}$ coincides with the body frame $\mathcal{B}$. The origin of the platform-fixed frame F also coincides with the origin B of the body frame, and for zero tip-and-tilt platform rotation angles $\nu_1 = \nu_2 = 0$, the frames $\mathcal{F}$ and $\mathcal{B}$ coincide.

Mass depletion is not simulated in this work: because mass flow rate of electric thrusters is typically small, it is reasonable to assume that significant CM shifts happen

over time scales that are much bigger than the time window in which the CM needs to be estimated. The goal for these simulations is to showcase the ability to estimate the CM location at thruster ignition, when the CM estimate might be inaccurate following a slew maneuver or a long coasting arc.

The LS algorithm to estimate the CM location is seeded with the initial guess $\boldsymbol{x}_0 = \{0.04, -0.05, 1.25\}^T$ and the initial state covariance $\boldsymbol{P}_0 = 0.0025[\boldsymbol{I}_{3\times3}]$, corresponding to a standard deviation of 5 cm along each component of the CM location.

7.2 Solar Radiation Pressure Modeling

For the purpose of SRP modeling, the spacecraft is represented as a collection of 10 facets with negligible thickness. Six square facets and four circular facets are used to model the rigid hub and solar arrays, respectively. The platform and thruster assembly are not considered for the SRP evaluation due to their relatively small size compared to the spacecraft hub and solar arrays.

Each facet is characterized by an area A, a vector normal to its surface $\hat{\boldsymbol{n}}$, a position vector from the spacecraft center of mass to the facet center of pressure, $\boldsymbol{r}_{P/C}$, and three optical coefficients representing the interaction of impinging photons with the facet surface. The fraction of specularly reflected, diffusely scattered, and absorbed photons are represented using the coefficients ρ, δ, and λ, respectively, where $\rho + \delta + \lambda = 1$.

The 6 spacecraft hub facets have areas of 2.7 m^2, 4.23 m^2, and 5.15 m^2. The array facets have an area of 41.42 m^2. The following optical coefficients are used for the hub:

$$\lambda_{\text{hub}} = 0.525 \qquad \rho_{\text{hub}} = 0.336 \qquad \delta_{\text{hub}} = 0.139 \tag{74}$$

and the solar arrays:

$$\lambda^+_{\text{sa}} = 0.680 \qquad \rho^+_{\text{sa}} = 0.160 \qquad \delta^+_{\text{sa}} = 0.160 \tag{75}$$

$$\lambda^-_{\text{sa}} = 0.440 \qquad \rho^-_{\text{sa}} = 0.0 \qquad \delta^-_{\text{sa}} = 0.560, \tag{76}$$

where the + and - superscripts indicate the front, power-generating surface, and the rear surface, respectively.

A faceted force model is used to estimate the SRP force acting on the spacecraft [35]:

$$\boldsymbol{F}_{\text{SRP}} = \sum_{i=1}^{10} \boldsymbol{F}_{\text{SRP}_i} = -P(|\boldsymbol{r}_{\text{sc}/\odot}|) \sum_{i=1}^{10} A_i \cos(\theta_i) \left[(1-\rho_i)\hat{\boldsymbol{s}} + 2\left(\frac{\delta_i}{3} + \rho_i \cos(\theta_i) \right) \hat{\boldsymbol{n}}_i \right] \tag{77}$$

where $\hat{\boldsymbol{s}}$ is the unit direction vector pointing radially towards the Sun from the spacecraft body-frame origin, θ is defined as the incidence angle between each facet normal vector and the Sun-direction vector, and $P(|\boldsymbol{r}_{sc/\odot}|)$ is the pressure acting on the spacecraft scaled by the spacecraft heliocentric distance. In this work, the spacecraft is orbiting at 0.67 Astronomic Units from the Sun, roughly corresponding to the Venusian

Table 1 Control gains and parameters used in the simulation

variable	value	unit
K	9	Nm
P	275	Nms
K_I	10^{-5}	$(\text{Nms}^2)^{-1}$
K_{SA}	1.25	Nm
P_{SA}	50	Nms
K_{PL}	0.5	Nm
P_{PL}	3	Nms
$\bar{\epsilon}$	10^{-6}	/

heliocentric radius. This results in a value of $P(|\boldsymbol{r}_{sc/\odot}|) = 1.0205316 \times 10^{-5}$ Pa. The vector quantities in Equation (77) are expressed in spacecraft principal body-frame components. The total torque acting about the spacecraft center of mass due to SRP is calculated by summing the torque contributions over all 10 facets:

$$\boldsymbol{L}_{\text{SRP},C} = \sum_{i=1}^{10} \boldsymbol{L}_{\text{SRP},C_i} = \sum_{i=1}^{10} \boldsymbol{r}_{P_i/C} \times \boldsymbol{F}_{\text{SRP}_i}. \tag{78}$$

7.3 Control Gains and Simulation Parameters

Table 1 contains a list of the control gains mentioned in Equation (1) 5 and (6), together with the tolerance for the CM Estimator, and the corresponding values used in the simulation. The control gains were tuned through simulation, with the aim to guarantee faster convergence of the articulated appendages (thruster platform and solar arrays) with respect to the convergence of the main hub attitude. Moreover, the gains of the hub control law K and P were tuned to ensure attitude convergence within a tolerance $\bar{\epsilon}$ in a time that is inferior to the platform actuation time (1 hour). This is done to ensure the validity of the equations of motion and controls presented in Section 2. Gain variations of $\pm 15\%$ with respect to the values presented in Table 1 do not produce appreciable variation in simulation results, highlighting robustness of the model to gain selection.

7.4 Simulation Framework

The spacecraft is simulated using the Basilisk Astrodynamics Simulation Framework[1]. Basilisk is an open-source software framework that can simulate complex spacecraft systems and behaviors. Its modular structure allows building blocks, named modules, to simulate individual spacecraft components and/or flight software processes. Modules exist as standalone segments of code, with minimal interconnections. The

[1] https://avslab.github.io/basilisk/

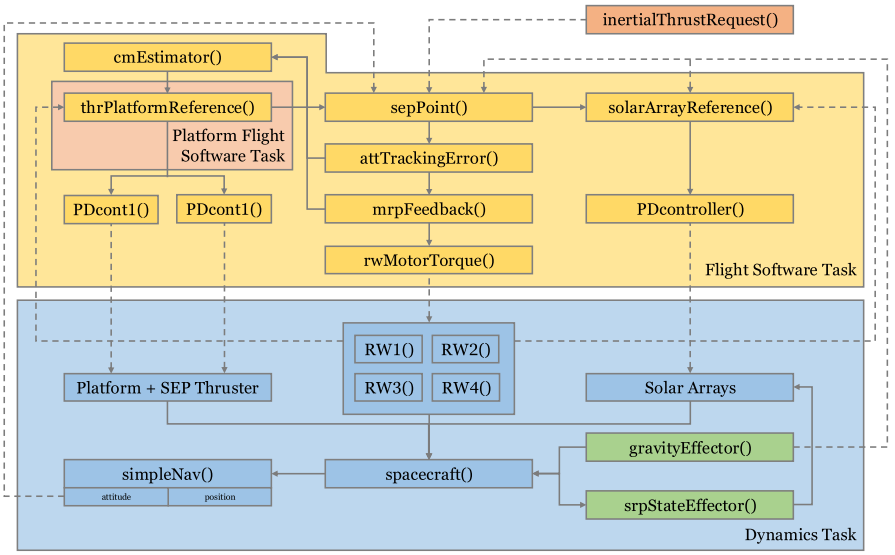

Fig. 9 Simulation block diagram

exchange of minimal information between modules limits the flow of information to what is strictly essential [40–42].

Figure 9 illustrates the most relevant modules that are used in the simulations carried out in this paper. The reader is referred to Calaon et al. [43] for a detailed description of what each code block represents within the simulation. It is noted that standard navigation filters for attitude and orbit determination are not modeled in this work, because they were considered out of the scope of this contribution. Instead, the `simpleNav` module adds noise to the propagated states to simulate noisy filter outputs that are fed to the flight software algorithms presented in this work.

The script used to generate these results can be found in the Basilisk Github repository[2]. A brief description of the scenario script and how to run it can be found in the examples folder on the Basilisk website[3]. In this work, the `platformReference` module is run at a slower frequency of 2.8×10^{-4} Hz (one update every hour), to ensure that the attitude is driven to the desired reference within the desired accuracy. In contrast, every other flight software segment is run at 1 Hz. The dynamics and the environment are run at a frequency of 10 Hz.

8 Results

This section presents the results obtained by simulating the spacecraft as described above, with the implementation of the control laws and flight software algorithms

[2] https://github.com/AVSLab/basilisk.git

[3] https://avslab.github.io/basilisk/examples/scenarioSepMomentumManagement.html

outlined. The following subsections implement such algorithms incrementally to show that the results correctly match the expected behavior for each module.

8.1 Perfect CM-thruster Alignment

This subsection aims to show the correct performance of the analysis outlined in Section 3. In this simulation, the proportional gain κ of the platform control law in Equation (32) is set to zero, to ensure that the thruster is indeed aligned with the provided system CM location. Moreover, the `cmEstimator` module is disconnected from the simulation, whereas the `platformReference` module is informed with the exact location of the system's CM: while this is not a realistic assumption for a real onboard computer, it serves the purpose of showing the performance of the guidance and control algorithms for the thruster platform. Figure 10 shows the most interesting results for this analysis: Figure 10(a) shows that the spacecraft attitude correctly tracks the generated reference. In Figure 10(c), the reference angles generated for the platform are constant throughout the simulation, and correctly tracked by the control law in Equation (6). This ensures that the thrust is continuously fired through the system CM, as shown by the thrust-to-CM offset angle in Figure 10(d). Such angle is the angle between the thrust vector $\boldsymbol{t}$ and the segment $\boldsymbol{r}_{C/T}$, connecting the thrust application point T to the real CM location. Figure 10(b) shows that, past the initial reaction wheel speed transient when the initial slew maneuver is performed, the wheel speeds grow linearly over time due to constant SRP torque acting on the system, as shown in Figure 10(e). Running this scenario for longer shows how, in the absence of any momentum management or momentum dumping maneuver, RW speeds can grow to almost 3000 rpm in four days exclusively due to SRP action. Lastly, Figure 10(f) shows the net external torques acting on the system, namely the sum of SRP and thruster torque, minus the SRP component about the thrust direction $\hat{\boldsymbol{t}}$, as expressed by Equation (68). As a consequence of aligning the thruster with the CM, the thruster torque with respect to the CM is zero, and therefore the only external torque acting on the system is produced by SRP.

8.2 Continuous SEP Momentum Management with perfect CM knowledge

The results in this subsection aim to show the performance of the momentum management strategy outlined in Section 4. The momentum management is delivered setting a gain $\kappa = 2.5 \times 10^{-4}$ Hz for the `platformReference` module. As in the previous subsection, this module receives the exact CM location as input. Figure 11 shows the results for this case. Figure 11(a) appears unchanged, even though small attitude reference variations happen at every hour, when the reference angles for the platform are being updated. This is better visualized in Figure 11(c), where the reference angle ν_{R1} undergoes three updates before settling to a steady state value. Figure 11(b) shows that, in this case, the wheel speeds are driven back to almost zero, showing the effectiveness of the control law in Equation (32) at feeding back on net RW momentum. As mentioned in in Section 4, the control law is under-actuated, and therefore momentum can still build up along the uncontrollable axis. However, with continuous momentum

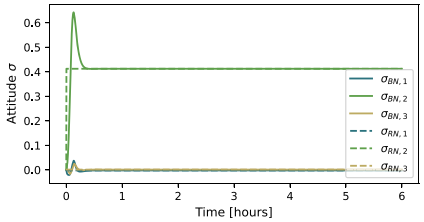

(a) Attitude and attitude reference vs time

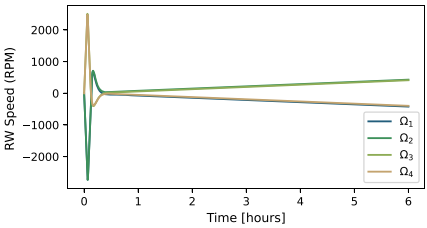

(b) Reaction wheel speeds vs time

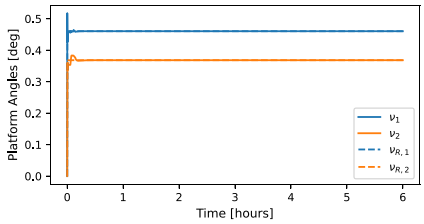

(c) Platform gimbal angles and references vs time

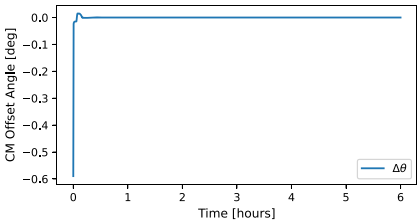

(d) Thrust-to-CM angle vs time

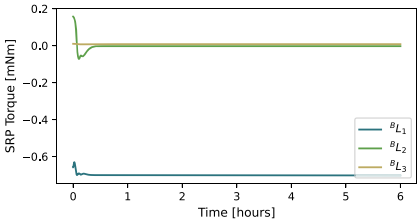

(e) SRP torque vs time

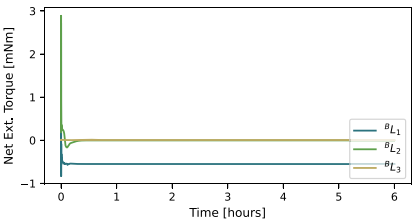

(f) Net external torques vs time

Fig. 10 Perfect CM-thruster alignment

management, wheel speeds remain within 50 rpm after 4 days. In Figure 11(d) it can be observed that the thruster settles at a constant angular offset with respect to the system CM: this is to ensure that the resulting thruster torque counteracts the SRP torque on the system. This is verified in Figure 11(f), which shows that the net external torques, minus the respective components along the thrust vector, are zero.

8.3 SEP- and SRP-based Momentum Management with Thruster Swirl Torque

Figure 12 shows the simulation results obtained when the SEP thruster is simulated including the effects of the swirl torque ($\chi \neq 0$). This simulation is run for 3 days to better appreciate the long-term effects of momentum buildup. After 1.5 days from ignition, the arrays are switched from power-generating mode to momentum management mode, as described in Section 5. Figure 12(b) shows the most evident results of this simulation: in the first 1.5 days the wheel momentum is building up along the positive $\hat{\boldsymbol{b}}_3$ direction, due to the swirl torque. The thruster is still unloading the

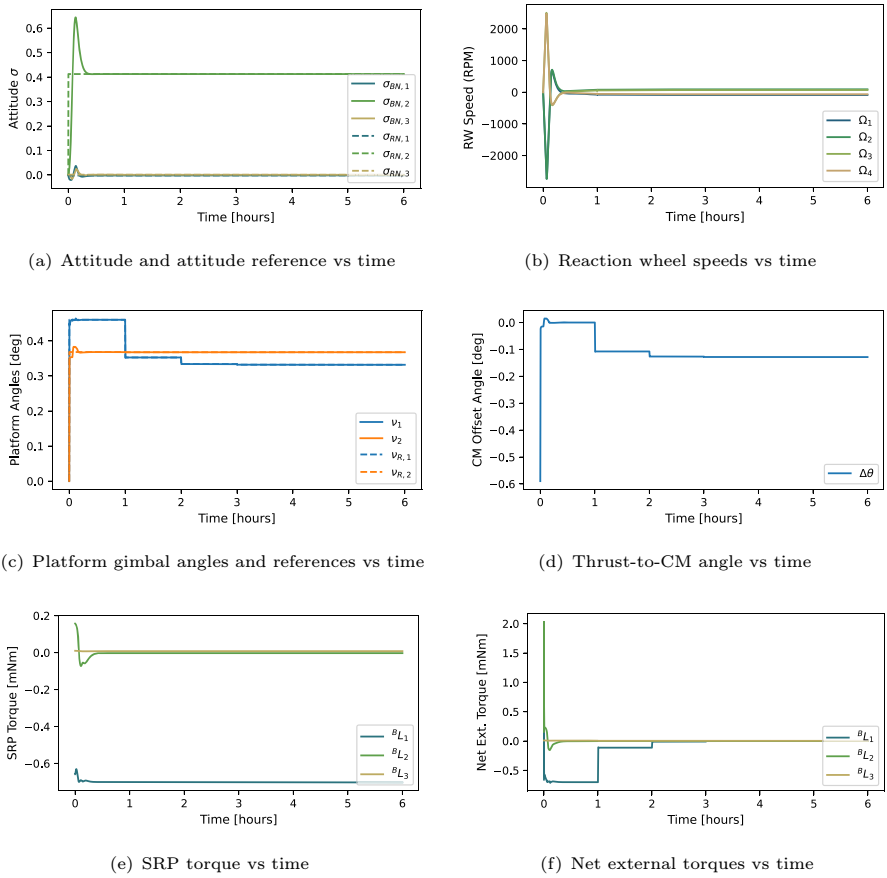

(a) Attitude and attitude reference vs time

(b) Reaction wheel speeds vs time

(c) Platform gimbal angles and references vs time

(d) Thrust-to-CM angle vs time

(e) SRP torque vs time

(f) Net external torques vs time

Fig. 11 Continuous momentum management with perfect CM knowledge

momentum building up due to SRP, but because the swirl torque is by definition about the thrust direction, this component of momentum cannot be unloaded by the thruster. The change in solar array pointing is shown in Figure 12(g) and 12(h). At $t = 1.5$ days, Figure 12(b) shows that a sharp decrease in the net momentum as a result of the SRP torque caused by the reorientation of one solar array. Equation (49) is used to compute the array deflection angle, with the following choice of tuning parameters: $\Theta = 2/3$, $n = 2$, and $\xi = 5 \cdot 10^{-5}$ $\mathrm{N}^{-2}\mathrm{m}^{-4}\mathrm{s}^{-2}$.

Figure 12(e) and 12(f) show that in the first half of the simulation the thruster torque is matching the SRP torque along the x and y axis, although the swirl torque is contributing a component along z. In the second half one array is deflected to counter the momentum build-up due to the swirl torque. Because of the deadband in the control law, the array settles at a 30 deg offset with respect to the Sun direction. Figure 12(d) highlights how, after the array deflection, the thruster is also immediately reoriented to respond to the variation of SRP torque along $\hat{\boldsymbol{b}}_1$ and $\hat{\boldsymbol{b}}_2$.

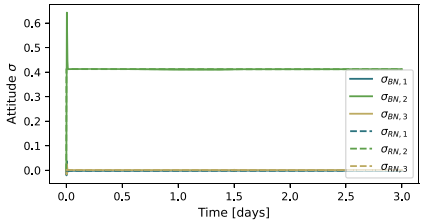

(a) Attitude and attitude reference vs time

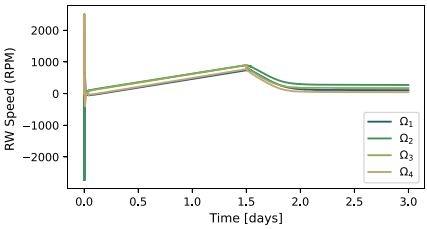

(b) Reaction wheel speeds vs time

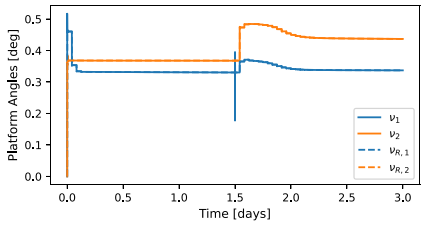

(c) Platform gimbal angles and references vs time

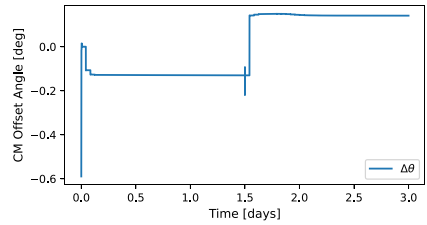

(d) Thrust-to-CM angle vs time

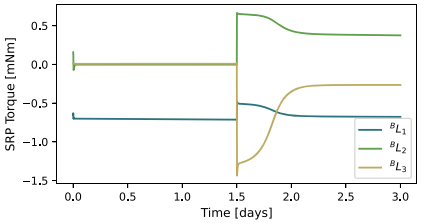

(e) SRP torque vs time

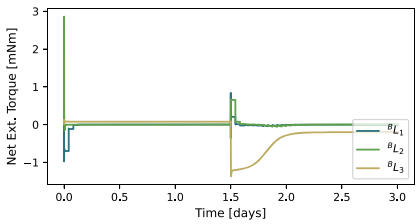

(f) Net external torques vs time

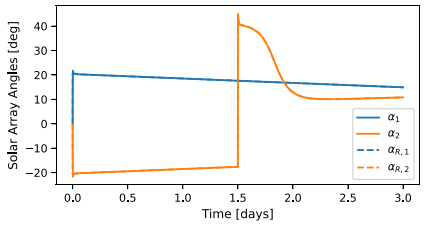

(g) Solar array angles and reference vs time

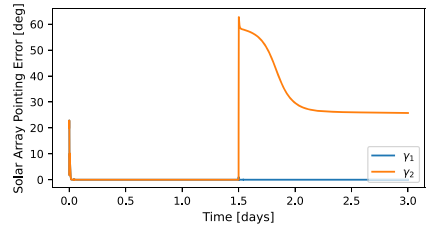

(h) Solar array Sun pointing vs time

Fig. 12 SEP- and SRP-based momentum management

8.4 Continuous Momentum Management with CM Uncertainty and Integral Feedback

This subsection presents the simulation results obtained by implementing an integral feedback term with gain $\kappa_I = 3 \cdot 10^{-9}$ Hz^2 in the platform control law in Equation (39). The flight software is seeded with the same initial CM estimate $\boldsymbol{x}_0$ presented

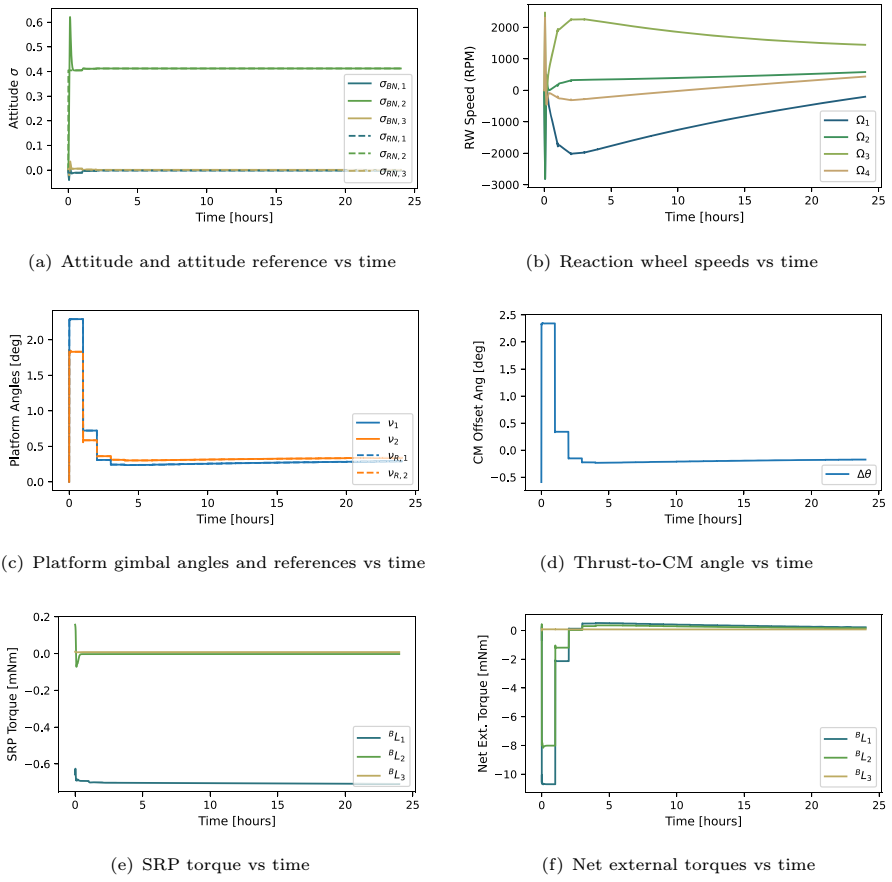

(a) Attitude and attitude reference vs time

(b) Reaction wheel speeds vs time

(c) Platform gimbal angles and references vs time

(d) Thrust-to-CM angle vs time

(e) SRP torque vs time

(f) Net external torques vs time

Fig. 13 Continuous momentum management with CM uncertainty and platform integral feedback

in Section 7.1. The results are presented in Figure 13. Figure 13(c) and 13(d) show that the platform quickly converges to a steady-state equilibrium, provided that the platform reference gains κ and κ_I are properly tuned. As in the previous section, this equilibrium consists of a configuration in which the SRP torque is compensated almost exactly by the thruster torque, as can be inferred from Figure 13(e) and 13(f). The main issue is that the introduction of the integral feedback term causes the momentum management control loop to become significantly underdamped. As a result, Figure 13(b) shows that the reaction wheels grow quickly during the transient response due to the misalignment between the thruster and CM. At steady state, the wheel speeds are progressively being reduced by the continuous momentum management action of the thruster.

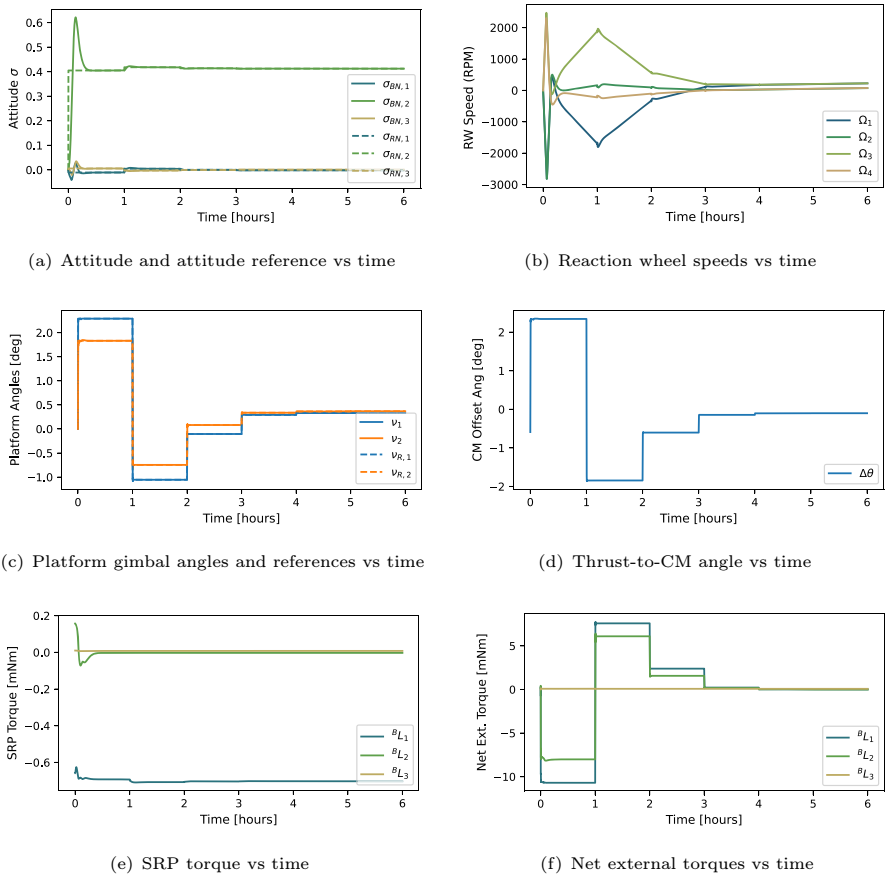

(a) Attitude and attitude reference vs time

(b) Reaction wheel speeds vs time

(c) Platform gimbal angles and references vs time

(d) Thrust-to-CM angle vs time

(e) SRP torque vs time

(f) Net external torques vs time

Fig. 14 Continuous momentum management with estimated CM

8.5 Continuous Momentum Management with Estimated CM

This last subsection shows the performance of the momentum management strategy combined with continuous CM estimation. The robustness of the `cmEstimator` module is tested with a relatively inaccurate initial guess on the CM location, as mentioned in Section 7.1. This has repercussions on all plots in Figure 14, where longer transients can be observed. Figure 14(a) shows that the reference attitude changes every hour: this is to ensure that, as the thruster platform is articulated to perform momentum management, the attitude is also steered to maintain the thruster aligned inertially. Figure 14(c) shows the more significant updates in the gimbal angles required to ensure continuous momentum management, while simultaneously updating the current estimate on the CM location. In Figure 14(b), RWs undergo larger transients while the CM location is not yet determined accurately: in the first hour the gimbal is aligned according to the inaccurate initial CM estimate, and this results in a large thruster torque imparted to the system and compensated by the RWs. With the second

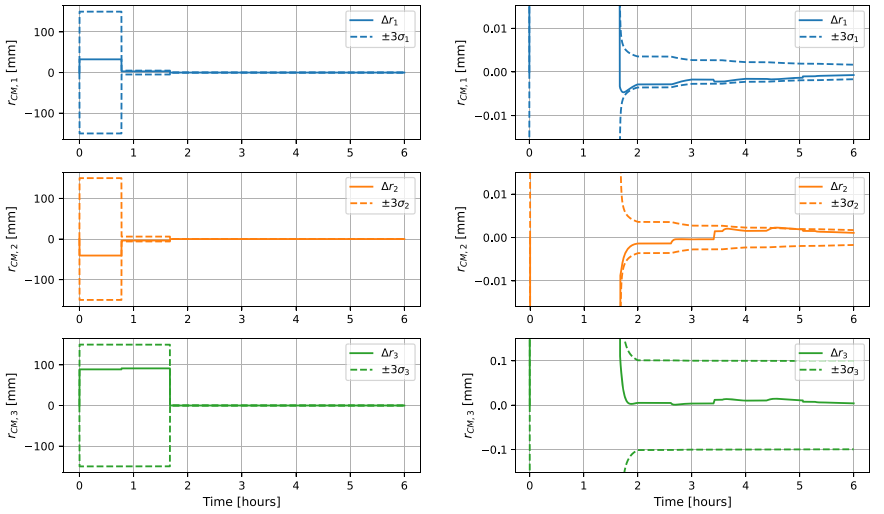

(a) State estimation error and covariance vs time (b) State estimation error and covariance vs time (zoom)

Fig. 15 State estimation error and covariance without SRP effect

and third measurement updates, occurring at $t = 2$ hours and $t = 3$ hours, respectively, the estimate on the CM location improves, and the system's behavior is dominated by the action of the momentum management control loop. After $t = 4$ hours the wheel speeds settle at a near constant rate, which is higher than the respective plot in Figure 11: this happens because in this scenario the wheels are spun up to absorb the transient thruster torques, and due to the under-actuated nature of the control law in Equation (32), the wheel speeds cannot be driven exactly to zero. Figure 14(d), coherently with Figure 14(c), shows larger oscillations of the thruster about the CM. However, the same steady state offset angle of $\Delta\theta = 0.05$ deg with respect to the CM location is reached as in Figure 11. Figure 14(e) shows that the SRP components vary every hour as attitude is adjusted. Finally, Figure 14(f) shows that, at steady state, the net external torques are balancing in the plane orthogonal to the thrust direction vector.

It is interesting to observe the results of the CM estimation algorithm used in this subsection, in comparison with the true CM location used in Section 8.1 to 8.3. Specifically, it is interesting to compare the performance of the algorithm when external perturbations (SRP) are present, and when they are not. When SRP effect is removed, the plots in Figure 14 do not change substantially. However, an impact can be seen when analyzing the errors of the estimated CM location compared to the truth.

8.5.1 CM Estimation without SRP Influence

The contribution of SRP is removed to generate the following results. The only source of error to the measurement model in Section 6 is due to the convergence error between actual attitude and reference attitude. The measurement noise covariance is set to $[\boldsymbol{R}] = 10^{-10}[\boldsymbol{I}_{3\times3}]\,\text{Nm}^2$. Figure 15 shows the estimated state errors and respective

3σ bounds. The two subfigures show the same results, in different scales. Figure 15(a) highlights the macroscopic behavior of the estimation algorithm in the first two hours of operation. It can be observed that the CM updates happens before the end hour, as soon as the convergence error ϵ drops below the threshold that triggers the measurement update. Beyond the initial measurement update, even though the algorithm keeps processing measurements, no significant updates happen, because the measurements are substantially identical until the requested gimbal angles are also updated at the hour mark. It is possible to observe that the second measurement update, happening just before $t = 2$ hours, is enough to drive the estimated state to a negligible error: this is consistent with the expectation that two linearly-independent torque measurements are enough to resolve the location of the CM. Beyond the second update, the estimate state barely varies. Figure 15(b) is interesting because it provides insight on the accuracy within which each state component can be estimated: it is possible to observe that, despite the fact that the initial state covariance is the same for all three CM coordinates, the 3σ bounds on the first two states in the end are an order of magnitude smaller than the bounds on the third component. This result is expected in this application in which the thrust vector is primarily aligned along the $\hat{\boldsymbol{b}}_3$ axis, because the thrust direction vector coincides with the non-observable direction. Regardless, the gimbaling of the thruster makes the problem globally observable, and the third coordinate of the CM location can be estimated with an accuracy of fractions of a millimeter.

8.5.2 CM Estimation with SRP Influence

SRP is added back to the simulation and the measurement noise covariance is increased to $[\boldsymbol{R}] = 4 \times 10^{-8}[\boldsymbol{I}_{3\times3}]$ Nm^2 to be consistent with the SRP torques observed in Figure 10, 11 and 14. The goal is to have the algorithm absorb the SRP contribution as measurement noise. From a macroscopic level the results are similar to Figure 15 (a), where after two measurement updates the estimate converges to the steady state value. However, Figure 16(a) shows that a steady state bias is present in the estimated state, particularly evident along the second and third CM coordinates. This happens despite the fact that the post-fit residuals in Figure 16(b) are well within the 3σ measurement noise covariance. This is a consequence of having a biased measurement model as described in Equation (69). As a result, the estimated state is not the real CM location, but rather the location of point C^* that drives the system to a steady state equilibrium. This is further validated by the fact that, despite the estimate being incorrect, the algorithm still drives the net external torques to zero as shown in Figure 14(f). In terms of the combined action of the `cmEstimator` module and the `platformReference` module, the first estimates the location of the "effective" CM that ensures the smallest amount of momentum build-up over time. The latter, on the other hand, receives the effective CM location C^* as an input, and consequently drives the thruster to a zero offset with respect to C^*.

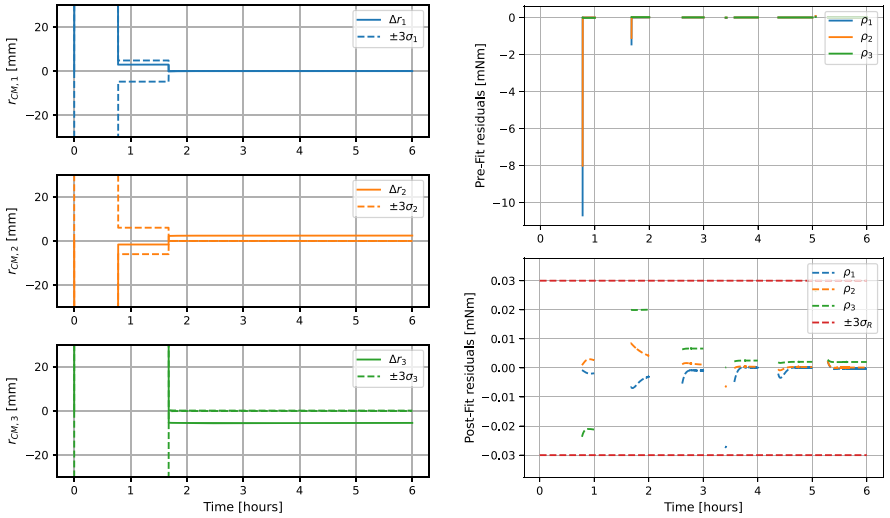

(a) State estimation error and covariance vs time

(b) Pre-fit and post-fit residuals vs time

Fig. 16 State estimation error and covariance, and residuals, with SRP effect

Table 2 Table of dispersed properties and initial conditions for MC runs

variable	distribution	bounds / std
m_{hub}	uniform	[2375, 2625] kg
$r_{C_{\text{hub}}/B}$	normal	5 cm - 3σ
$[\boldsymbol{J}_{\text{hub}}]$	normal	5% - 3σ
$\mathcal{B}\hat{\boldsymbol{u}}_i$	normal	2 deg - 3σ
$\Omega_i(0)$	uniform	[-1000, 1000] rpm
$J_{\text{ws},i}$	uniform	[0.1512, 0.1671] kg m^2
$m_{\text{sa},i}$	uniform	[80.75, 89.25] kg m^2
$[\boldsymbol{J}_{\text{sa}_s,i}]$	normal	5% - 3σ
$\|\boldsymbol{t}\|$	uniform	[0.513, 0.567] N
$\hat{\boldsymbol{t}}$	normal	0.5 deg - 3σ
$\boldsymbol{x}_0$	uniform	5 cm - 3σ

8.6 Monte Carlo Results

This final set of results is provided to show the robustness of the simulation to dispersed initial conditions and with variations in mass and inertia properties not modeled in the flight software. The following initial conditions are dispersed in 500 Monte Carlo runs, with respect to the nominal values already presented in Section 7 (Table 2):

Figure 17(a) and 17(b) display the simulated behavior of reaction wheels and solar arrays for a scenario where concurrent SEP thruster and solar array momentum management are performed. At 1.5 days of simulation time, the arrays are switched from power generation mode to momentum management mode. The SEP thruster's swirl

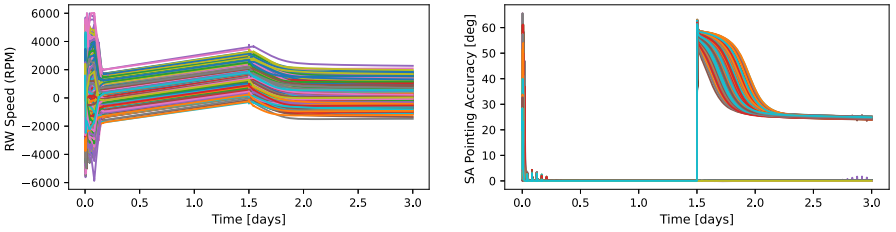

(a) Reaction Wheel Speeds (b) Solar array Sun pointing

Fig. 17 Monte Carlo Runs

torque disturbance is being modeled. The uncertainty on the CM is twofold, because dispersions are added to both the real CM location and the initial CM guess $\boldsymbol{x}_0$. The CM estimation algorithm is used to drive the system to a stable configuration. Figure 17(a) displays large initial RW transients: this is explained by the large number of dispersions injected into the Monte Carlo runs: when the algorithm starts on loaded wheels and a poor initial CM guess, the first iterations can cause the wheels speeds to grow. Such an undesirable situation is simulated here to test the strength of the proposed approach: it can be observed that, in a matter of a few hours, the wheels recover the linear trend due to the continuous injection of momentum from the SEP swirl torque. The spread in the RW speeds is due to different initial conditions, which result in different amounts of momentum along the uncontrollable thrust direction vector at steady state. At $t = 1.5$ days the RW momentum is reduced due to the momentum-offloading action of one of the arrays. Coherently, Figure 17(b) shows the actuation of one solar array to perform momentum management about the thrust direction vector.

9 Conclusions

This paper presents a general analytical solution on how to use a solar electric propulsion thruster mounted on a gimbaled platform and single-hinge rotating solar arrays attached to the spacecraft hub to perform continuous momentum management for a spacecraft on an interplanetary trajectory. This work starts from modeling the dual-gimbaled thruster platform assembly in a general manner, and delivering a closed-form solution to compute a guidance law for the reference tip and tilt angles required to control the platform. This is done to ensure the desired thruster torque performance. Subsequently, this paper presents a control law to offset the thrust vector with respect to the system center of mass, whose location is assumed known until this point. The control law feeds back on reaction wheel net momentum to deliver a thruster torque that counters momentum build-up. As a result, reaction wheel speeds barely grow over time, as opposed to noticeable linear growth without active momentum management. Similarly, a control law is derived to off-point the solar arrays from the incoming sunlight to leverage the differential solar radiation pressure torque to also perform momentum management on the spacecraft. The stability of both these control laws is proved using nonlinear control theory, and it is guaranteed under the satisfaction

of a set of reasonable assumptions presented along the derivation of the control laws. Lastly, this paper investigates the problem of center of mass estimation, necessary in order for the feedback control law to operate properly. It is shown that under the assumptions that the attitude reference frame does not vary significantly over a time window of a few hours, it is possible to exploit stabilizing integral feedback torque measurements to triangulate the location of the center of mass of the system. While this problem is, in principle, not fully observable, it becomes observable when multiple linearly-independent torque measurements are obtained orienting the thruster in different directions. For this measurement model to work, enough time needs to be allowed to the attitude control system to drive the spacecraft hub to the desired reference. Moreover, the integral feedback term is accurately linearly correlated to the thruster torque only under the assumption that the spacecraft reference attitude remains approximately constant. Lastly, results show that a bias appears in the estimated center of mass location when unmodeled external perturbations are acting on the system. Interestingly, this does not affect the steady-state performance of the system because the combined action of the estimation algorithm and the control law drive the thruster to the same CM offset as in the case in which perfect CM knowledge is assumed.

Acknowledgements Support for this effort was provided by the Emirates Mission to the Asteroid Belt (EMA), which is led by the UAE Space Agency in collaboration with the Laboratory for Atmospheric and Space Physics at the University of Colorado Boulder as its knowledge partner.

Author Contributions R.C. wrote the main manuscript and developed the Guidance and Control equations discussed in this contribution as part of his PhD research. C.A. advised on this work through regular discussions on its relevance to the Emirates Mission to the Asteroid Belt (EMA). H.S. served as the primary author's dissertation advisor. Both C.A. and H.S. reviewed the manuscript.

Data Availability No datasets were generated or analysed during the current study.

Code Availability The script used to generate these results can be found in the Basilisk Github repository at https://avslab.github.io/basilisk/examples/scenarioSepMomentumManagement.html

Declarations

Conflict of Interest The authors declare no conflict of interest.

References

1. Holste, K., Dietz, P., Scharmann, S., Keil, K., Henning, T., Zschätzsch, D., Reitemeyer, M., Nauschütt, B., Kiefer, F., Kunze, F.: Ion thrusters for electric propulsion: scientific issues developing a niche

technology into a game changer. Rev. Sci. Instrum. **91**(6), 061101 (2020). https://doi.org/10.1063/5.0010134
2. Früh, C., Kelecy, T.M., Jah, M.K.: Coupled orbit-attitude dynamics of high area-to-mass ratio (hamr) objects: influence of solar radiation pressure, earth's shadow and the visibility in light curves. Celest. Mech. Dyn. Astron. **117**, 385–404 (2013). https://doi.org/10.1007/s10569-013-9516-5
3. Schaub, H., Junkins, J.L.: Nonlinear spacecraft stability and control. In: Analytical Mechanics of Space Systems, 4th edn. American Institute of Aeronautics and Astronautics Inc, Reston, Virginia (2018). Chap. 8.7. https://doi.org/10.2514/5.9781624105210.0387.0518
4. Banerjee, A.K., Pedreiro, N., Singhose, W.E.: Vibration reduction for flexible spacecraft following momentum dumping with/without slewing. J. Guid. Control. Dyn. **24**(3), 417–427 (2001). https://doi.org/10.2514/2.4737
5. Pedreiro, N.: Spacecraft architecture for disturbance-free payload. J. Guid. Control. Dyn. **26**(5), 794–804 (2003). https://doi.org/10.2514/2.5114
6. Karami, M.A., Sassani, F.: Spacecraft momentum dumping using fewer than three external control torques. J. Guid. Control. Dyn. **32**(1), 242–247 (2009). https://doi.org/10.2514/1.35616
7. Tong, D.: Spacecraft momentum dumping using gravity gradient. J. Spacecr. Rocket. **35**(5), 714–717 (1998). https://doi.org/10.2514/2.3389
8. Hogan, E.A., Schaub, H.: Three-axis attitude control using redundant reaction wheels with continuous momentum dumping. J. Guid. Control. Dyn. **38**(10), 1865–1871 (2015). https://doi.org/10.2514/1.g000812
9. Rayman, M.D., Fraschetti, T.C., Raymond, C.A., Russell, C.T.: Dawn: A mission in development for exploration of main belt asteroids vesta and ceres. Acta Astronaut. **58**(11), 605–616 (2006). https://doi.org/10.1016/j.actaastro.2006.01.014
10. Racca, G., Whitcomb, G., Foing, B.: The SMART-1 mission. ESA Bull. , 95 (1998)
11. Oh, D.Y., Collins, S., Drain, T., Hart, W., Imken, T., Larson, K., Marsh, D., Muthulingam, D., Snyder, J.S., Trofimov, D., et al.: Development of the Psyche mission for NASA's Discovery Program. Jet Propulsion Laboratory, National Aeronautics and Space Administration, Pasadena, CA (2019)
12. Calaon, R., Allard, C., Schaub, H.: Solar electric propulsion GN&C pointing state overview for the Emirates Mission to the Asteroid Belt. In: AAS Guidance, Navigation, and Control Conference, Breckenridge, CO, USA (2024). Paper No. AAS-24-056
13. Kiner, L., Allard, C., Schaub, H.: Two-axis gimbal simulation overview for the Emirates Mission to the Asteroid Belt. In: AAS Guidance, Navigation, and Control Conference, Breckenridge, CO, USA (2025) . (Paper No. AAS-25-013)
14. Oh, D.Y., Collins, S., Randolph, T.M., Vanelli, C., Tilley, S.: Feasibility of All-Electric Three Axis Momentum Management for Deep Space Small Body Rendezvous. In: 50th AIAA/ASME/SAE/ASEE Joint Propulsion Conference, Cleveland, OH, USA (2014). https://doi.org/10.2514/6.2014-3906
15. Pizzetti, A., Rizza, A., Topputo, F.: Autonomous wheel off-loading strategies for deep-space cubesats. Aerotec. Missili Spaz. **102**(1), 3–15 (2023). https://doi.org/10.1007/s42496-022-00137-2
16. Kawaguchi, J., Kominato, T., Shirakawa, K.: Attitude control flight experience: Coping with solar radiation and ion engines leak thrust in Hayabusa (MUSES-C). In: Proceedings of the 20th International Symposium on Space Flight Dynamics, Annapolis, MD, USA (2007)
17. Kornienko, A., Harris, R.S., Temporelli, P., Ho, K.: Disturbance torque compensation of the Bepi-Colombo spacecraft during interplanetary cruise flight using solar sailing effect. In: AIAA Guidance, Navigation, and Control (GNC) Conference, Boston, MA, USA (2013). https://doi.org/10.2514/6.2013-5120
18. Bergmann, E., Walker, B.K., Levy, D.R.: Mass property estimation for control of asymmetrical satellites. J. Guid. Control. Dyn. **10**(5), 483–491 (1987). https://doi.org/10.2514/3.20243
19. Bergmann, E., Dzielski, J.: Spacecraft mass property identification with torque-generating control. J. Guid. Control. Dyn. **13**(1), 99–103 (1990). https://doi.org/10.2514/3.20522
20. Kim, D.-H., Choi, D.-G., Oh, H.-S.: Inertia estimation of spacecraft based on modified law of conservation of angular momentum. J. Astron. Space Sci. **27**(4), 353–357 (2010). https://doi.org/10.5140/jass.2010.27.4.353
21. Tanygin, S., Williams, T.: Mass property estimation using coasting maneuvers. J. Guid. Control. Dyn. **20**(4), 625–632 (1997). https://doi.org/10.2514/2.4099
22. Ma, O., Dang, H., Pham, K.: On-orbit identification of inertia properties of spacecraft using a robotic arm. J. Guid. Control. Dyn. **31**(6), 1761–1771 (2008). https://doi.org/10.2514/1.35188

23. Allard, C., Ramos, M.D., Schaub, H., Kenneally, P., Piggott, S.: Modular software architecture for fully coupled spacecraft simulations. J. Aerosp. Inf. Syst. **15**(12), 670–683 (2018). https://doi.org/10.2514/1.i010653
24. Schaub, H., Junkins, J.L.: Stereographic orientation parameters for attitude dynamics: a generalization of the Rodrigues parameters. J. Astronaut. Sci. **44**(1), 1–19 (1996)
25. Krishnan, S., Vadali, S.R.: An inverse-free technique for attitude control of spacecraft using CMGs. Acta Astronaut. **39**(6), 431–438 (1996). https://doi.org/10.1016/s0094-5765(96)00152-x
26. Calaon, R., Allard, C., Schaub, H.: Attitude reference generation for spacecraft with rotating solar arrays and pointing constraints. Astrodynamics **9**(3), 389–406 (2025). https://doi.org/10.1007/s42064-024-0245-1
27. Sidi, M.J.: Spacecraft Dynamics and Control: a Practical Engineering Approach. Cambridge University Press, Cambridge, U.K. (1997). Chap. 7.3
28. Alcorn, J., Allard, C., Schaub, H.: Fully coupled reaction wheel static and dynamic imbalance for spacecraft jitter modeling. J. Guid. Control. Dyn. **41**(6), 1380–1388 (2018). https://doi.org/10.2514/1.g003277
29. Allard, C., Schaub, H., Piggott, S.: General hinged rigid-body dynamics approximating first-order spacecraft solar panel flexing. J. Spacecr. Rocket. **55**(5), 1291–1299 (2018). https://doi.org/10.2514/1.a34125
30. Vaz Carneiro, J., Allard, C., Schaub, H.: General dynamics for single-and dual-axis rotating rigid spacecraft components. J. Spacecr. Rocket. **61**(4), 1099–1113 (2024). https://doi.org/10.2514/1.A35865
31. Kiner, L., Schaub, H., Allard, C.: Spacecraft backsubstitution dynamics with general multibody prescribed subcomponents. J. Aerosp. Inf. Syst **22**(8), 703–715 (2025). https://doi.org/10.2514/1.I011491
32. Rodrigues, O.: Des lois géométriques qui régissent les déplacements d'un système solide dans l'espace, et de la variation des coordonnées provenant de ces déplacements considérés indépendamment des causes qui peuvent les produire. Journal de mathématiques pures et appliquées **5**, 380–440 (1840)
33. Khalil, H.K.: Nonlinear Systems, 3rd edn. Prentice Hall, Upper Saddle River, NJ, United States (2002). Chap. 4.1
34. Mukherjee, R., Chen, D.: Asymptotic stability theorem for autonomous systems. J. Guid. Control. Dyn. **16**(5), 961–963 (1993). https://doi.org/10.2514/3.21108
35. Rodriguez-Solano, C.J., Hugentobler, U., Steigenberger, P.: Adjustable box-wing model for solar radiation pressure impacting gps satellites. Adv. Space Res. **49**(7), 1113–1128 (2012). https://doi.org/10.1016/j.asr.2012.01.016
36. Henninger, R.J.: Solar absorptance and thermal emittance of spacecraft materials. NASA reference publication 1121, National Aeronautics and Space Administration (1984). https://ntrs.nasa.gov/citations/19840015630
37. Simon, D.: Optimal State Estimation: Kalman, H Infinity, and Nonlinear Approaches. John Wiley & Sons, Hoboken, NJ, United States (2006). Chap. 1.7. https://doi.org/10.1002/0470045345
38. Sontag, E.D.: Mathematical Control Theory: Deterministic Finite Dimensional Systems, 2nd edn. Springer, New York, NY (1998). Chap. 6.3. https://doi.org/10.1007/978-1-4612-0577-7_6
39. Snyder, J.S., Chaplin, V.H., Goebel, D.M., Hofer, R.R., Ortega, A.L., Mikellides, I.G., Kerl, T., Lenguito, G., Aghazadeh, F., Johnson, I.: Electric Propulsion for the Psyche Mission: Development Activities and Status. In: AIAA Propulsion and Energy 2020 Forum, Virtual Event (2020). https://doi.org/10.2514/6.2020-3607
40. Kenneally, P.W., Piggott, S., Schaub, H.: Basilisk: a flexible, scalable and modular astrodynamics simulation framework. J. Aerosp. Inf. Syst **17**(9), 496–507 (2020). https://doi.org/10.2514/1.i010762
41. Carnahan, S., Piggott, S., Schaub, H.: A new messaging system for basilisk. In: AAS Guidance, Navigation, and Control Conference, Breckenridge, CO, USA (2020). Paper No. AAS 20–134
42. Cols-Margenet, M., Schaub, H., Piggott, S.: Modular attitude guidance: generating rotational reference motions for distinct mission profiles. J. Aerosp. Inf. Syst **15**(6), 335–352 (2018). https://doi.org/10.2514/1.i010554
43. Calaon, R., Kiner, L., Allard, C., Schaub, H.: Momentum management of a spacecraft equipped with a dual-gimballed electric thruster. In: AAS Guidance, Navigation, and Control Conference, Breckenridge, CO, USA (2023). (Paper No. AAS-23-178)